UNIVERSITY OF CALIFORNIA,
IRVINE

Multi-Decadal Contemporary Sea Level Changes from Land-Ice Derived Using Satellite Observations and Climate Model Outputs

DISSERTATION

submitted in partial satisfaction of the requirements
for the degree of

DOCTOR OF PHILOSOPHY

in Earth System Science

by

Zhuoya He

Dissertation Committee:
Professor Isabella Velicogna, Chair
Professor Eric Rignot
Professor Mathieu Morlighem

2021

DEDICATION

To my parents

TABLE OF CONTENTS

LIST OF FIGURES

LIST OF TABLES

ACKNOWLEDGMENTS

Throughout the writing of the dissertation, I have received a great deal of support and assistance.

I would first like to thank my advisor, Professor Isabella Velicogna, whose expertise was invaluable in formulating the research questions and methodology. Thank you for your guidance through each stage of the process. Thank you for always checking up and showing how much you care about me.

I would like to thank my committee members, Professor Eric Rignot and Professor Mathieu Morlighem. Your insightful feedback pushed me to sharpen my thinking and brought my work to a higher level.

I would like to acknowledge my coauthors and former group members, Enrico, Chia-Wei, and Yara. I am extremely grateful to have had the opportunity to work with you. You are instrumental in defining the path of my research.

I would also like to thank my fellow group members, Geruo, Chia-Chun, Swetha, and Collin, and my first-year cohort. You made my Ph.D. journey incredibly rewarding.

I would like to thank my parents though words cannot express how thankful I am to have you as my parents! I am grateful to Meng, my boyfriend, who is always there for me throughout the ups and downs. Thank you, my friends, from college and the UCI Lamb fellowship. I couldn't have made it through the most challenging time without you.

Last but not least, I would like to thank the Earth System Science Department and the Jenkin's family for supporting my fellow graduate students and me.

This work was performed at the University of California, Irvine. This research was supported by the NASA's grant to Professor Isabella Velicogna.

VITA

Zhuoya He

EDUCATION

Doctor of Philosophy in Earth System Science **2021**
University of California Irvine *Irvine, California*

Master of Science in Earth System Science **2017**
University of California Irvine *Irvine, California*

Bachelor of Science in Marine Sciences **2016**
Ocean University of China *Qingdao, Shandong*

RESEARCH EXPERIENCE

Graduate Research Assistant **2016–2021**
University of California, Irvine *Irvine, California*

TEACHING EXPERIENCE

Instructor of Record **Summer 2021**
University of California, Irvine *Irvine, California*

Teaching Assistant **2018–2021**
University of California, Irvine *Irvine, California*

PUBLICATIONS AND CONFERENCE PRESENTATIONS

Four Decades of Measurement-Based Sea Level Fingerprints of Land-Ice. In submission. **2021**
Geophysical Research Letters

Reconstruction of 36-Year Measurement-Based Sea Level Fingerprints from Land-Ice Mass Changes. **2019**
American Geophysical Union Fall Meeting

Four decades of observation-based land-ice sea level fingerprints. **2019**
GRACE and GRACE-FO Science Meeting

Improved regional sea-level estimates from Ice Sheets, Glaciers, and Ice Caps using GRACE time series and other data. **2018**
American Geophysical Union Fall Meeting

SKILLS

Programming and statistical tools: Python, R, MATLAB, Fortran

Data analysis: satellite remote sensing, GIS, numerical climate models, in-situ measurements

Systems: LINUX

FELLOWSHIP AND AWARDS

Outstanding Teaching Assistant Department Awards 2021

Second Prize for the 6th Annual Elevator Pitch Competition 2020

Nominated for Most Promising Future Faculty Award 2019

Earth System Science Fellowship 2016

ABSTRACT OF THE DISSERTATION

Multi-Decadal Contemporary Sea Level Changes from Land-Ice Derived Using Satellite Observations and Climate Model Outputs

By

Zhuoya He

Doctor of Philosophy in Earth System Science

University of California, Irvine, 2021

Professor Isabella Velicogna, Chair

We reconstruct a historical sea level record due to land ice mass changes over the past four decades (1980-2019). Land ice includes polar ice sheets and mountain glaciers and ice caps (GIC). We estimate ice sheet mass changes using a Mass Budget Method, which compares surface mass balance at the interior of Greenland and Antarctica Ice sheets with ice discharge at the peripheral. For glaciers and ice caps, we extend mass changes observations from GRACE (Gravity Recovery and Climate Experiment) and GRACE-Follow On satellites with surface mass balance output products from state-of-art global and regional climate models. In the construction of the forty-year GIC record, we thoroughly account for uncertainties from different sources and correct trend bias in the climate models. We calculate global and regional sea level in response to the land ice mass changes. Land ice mass variations at different locations lead to a non-uniform sea level pattern called sea level fingerprints (SLF). Our record triples the previous observation period of SLF estimates based on GRACE/GRACE-FO alone, improving confidence in the estimates during the common period. Over the past four decades, the GIC contributed a larger mass loss than Greenland and Antarctica, but with minor differences between them. We use the reconstructed land ice sea level record combined with other sea level components to further study the closure of the sea level budget during the recent 15 years (2005-2019). We examine the closure

of sea level budget by comparing the total sea level measured by altimetry to the sum of individual sea level components, including steric sea level and SLF induced by mass changes from land water and atmospheric and oceanic non-tidal dynamical processes. We find an excellent agreement between the sum and the total sea level at the global mean scale and in the Pacific Ocean, which suggests closure of sea level at the majority of the global ocean during 2005-2019. The dominant signals are from ice sheets and steric components for the past forty years, but the GIC signal remains significant and cannot be ignored. We expect the 40-year SLF record and the evaluation on the recent 15 years' sea level budget to be of importance to help constrain model physical processes and, in turn, enhance projections of future sea level rise.

Chapter 1

Introduction

Sea level rise is a direct indicator of climate change. Sea level is rising and will continue to rise for centuries [*Oppenheimer et al.*, 2019]. Contemporary global mean sea level rise is primarily caused by land ice melting and ocean warming [*Cazenave et al.*, 2018b, a]. Land ice also drives long-term, large-scale spatial variability in the regional sea level [*Frederikse et al.*, 2020b]. Ocean warming changes the ocean volume and causes sea level changes on the global and regional scales. Terrestrial water storage variations, atmospheric pressure changes, and ocean dynamical movements (e.g., tides, currents) can also change sea levels.

Land ice includes polar ice sheets (i.e., Greenland and Antarctic ice sheets, mountain glaciers, and ice caps). The projections of land ice mass changes and the corresponding sea level rise have considerable uncertainty [*Kopp et al.*, 2014]. Reliable long-term observations are needed to reduce this model uncertainty and help deliver accurate projections. Reconstruction approaches for ice sheets include altimetry [*Csatho et al.*, 2014; *McMillan et al.*, 2016], GRACE satellites [*Velicogna et al.*, 2020; *Velicogna and Wahr*, 2013], mass budget method [*Rignot et al.*, 2019; *Mouginot et al.*, 2019], and a reconciliation between different methods citepshepherd2012reconciled. Previous methods to reconstruct glaciers' mass balance include

extrapolation of sparse field data [*Meier*, 1984], reconstruction using climatology [*Dyurgerov and Meier*, 2000], and mass changes derived from elevation changes obtained at various periods and interpolating in between [*Kaser et al.*, 2006; *Zemp et al.*, 2019]. Previous long-term records for glaciers and ice caps mostly rely on extrapolating sparse measurements which are not observed continuously in space or time, which comes with significant errors.

Mass changes in the land ice alter the global averaged sea level and lead to a unique spatial distribution of the sea level, which is referred to as the "sea level fingerprints" or the "self-attraction and loading effect" [*Riva et al.*, 2010; *Wouters et al.*, 2011; *Hughes et al.*, 2012]. Each mass change source can produce a distinct sea level pattern where sea level increases in the field far away from the source location and sea level drops in the nearby area. This pattern is a collective impact from the earth's gravitational, rotational, and deformational response to mass changes.

The theory of sea level fingerprint has been established for over four decades since 1976 when *Farrell and Clark* [1976] first introduced the sea level pattern which would happen on deformable earth in response to gravitational changes. Then in 1977, *Clark and Lingle* [1977] specifically discussed how ice sheets melting could influence the sea level fingerprint pattern. *Clark and Lingle* [1977] used the same equation from *Farrell and Clark* [1976] and calculated sea level fingerprint in response to melting of the West Antarctic ice sheet with an assumption of a uniform melting across the West Antarctic ice sheet. Ten years later, *Clark and Primus* [1987] predicted sea level fingerprints caused by ice sheets mass loss under a future warming climate. Both the 1977 and 1987 studies identified a sea level fall near the sources of ice mass loss and a rise in the far-field. Another ten years later, mountain glaciers were for the first time being considered together with the polar ice sheets to compute the sea level fingerprints in *Conrad and Hager* [1997]. Again, this study is based on an assumed ice mass distribution. When it came to the 21st century, the phenomenon of this non-uniform sea level pattern resulting from mass changes got more recognition. In particular, *Mitrovica*

et al. [2001] and *Tamisiea et al.* [2001] further developed the sea level fingerprint theory to include the impact of the earth's rotation which accounts for about 10% of the signal [*Adhikari et al.*, 2019]. Later on, *Mitrovica et al.* [2009], *Bamber et al.* [2009], *Gomez et al.* [2010] further extended the theory to account for the impacts of migrations of shoreline.

Ignoring the spatial variability in the mass loading field would lead to considerable errors in the resulting sea level fingerprint [*Hsu and Velicogna*, 2017]. While SLF results based on realistic land ice mass changes spatial distribution only became available in recent two decades since the satellite gravimetry period (e.g., [*Riva et al.*, 2010], [*Wouters et al.*, 2011], [*Hsu and Velicogna*, 2017], [*Adhikari et al.*, 2019]). Gravity Recovery and Climate Experiment (GRACE) satellites and their successors, the GRACE-Follow On (hereafter refers to GRACE-FO) satellites, have been measuring the earth's gravity field changes on a monthly scale since 2002. Land-mass changes can be derived from the GRACE observations according to Newton's Law of Universal Gravitation. The associated sea level changes can be calculated using the mass changes as the input fields to solve the Sea Level Equations [*Hsu and Velicogna*, 2017].

Our study reconstructed a land ice SLF record based on realistic land ice mass changes for the past four decades. To our knowledge, this is the first long-term SLF based on realistic monthly land ice mass changes spatial fields. We combine satellite observations and climate model outputs to increase spatial and temporal coverage of land ice and the associated sea level records. Chapter 2 will detail existing reconstruction methods and our novel approach that leverages multiple satellites, global and regional climate models to generate a consistent four-decade land-ice mass changes record from 1980 to 2019 and the associated robust error analysis. A long-term record of land ice and the associated sea level changes and thorough error estimates will help constrain model processes and improve model prediction accuracy. Our SLF record also enables detection of the SLF signal at tide gauge locations. The detection is of particular interest among oceanography and climate science studies, as direct

observation-based evidence of SLF is rare despite the fact the theory has been accepted for over four decades. Our forty-year, monthly record of SLF will permit detections of the signal at various temporal and spatial scales, further demonstrating the significance of this non-uniform sea level pattern in response to land-ice melting under a warming climate [*Von Schuckmann et al.*, 2016b].

Based on the most up-to-date observations, we also reassessed the global and regional sea level budget for the recent two decades (2002-2019). We continue to use the land-ice induced SLF record as we reconstructed in Chapter 2 combined with other individual sea level contributions and compare them to the total sea level. These individual sea level contributors include steric sea level computed using oceanic temperature and salinity observations from ARGO floats, land-water induced SLF, and atmospheric and non-tidal ocean loading induced SLF. The total sea level changes are sea surface height measured by altimetry. We evaluated the sea level budget by comparing two approaches that determine the total change in sea level. The first approach is to directly measure the total sea level, or sea surface height changes, using tide gauges or satellite altimetry. The second approach is to quantify individual sea level components separately. When the sum of the individual parts agrees with the total sea level obtained from the first approach, the sea level budget is considered "closed". A closed or a balanced sea level budget can be expressed as the following equation:

$$SL_{Total} = SL_{LandIce} + SL_{LandWater} + SL_{Steric} + SL_{AtmosPres} + SL_{OceanDyn} \tag{1.1}$$

Where SL_{Total}, $SL_{LandIce}$, $SL_{LandWater}$, SL_{Steric}, $SL_{AtmosPres}$, $SL_{OceanDyn}$, are total sea level, sea level caused by land ice mass changes, sea level caused by land water storage changes, sea level caused by ocean density changes (i.e., steric sea level), sea level caused by atmospheric pressure changes, sea level caused by dynamical ocean processes, and uncertainties.

A closed sea level budget over specific periods indicates that the observed contributors can

fully explain the change in the overall sea level [*Cazenave et al.*, 2018b]. A better understanding of what processes controls sea level changes will help improve model physics and the accuracy of future sea level predictions. For example, altimetry measured sea level rise over 1993-2018 at a rate of 3.35 mm per year, more than double the rate in 1900-2018, which is 1.53 mm per year *Frederikse et al.* [2020b]. Interpreting the causes of this accelerated sea level rise requires investigation on individual contributors. While high-quality total sea level measurements date back to the 1990s, observations on ocean thermostatic changes induced sea level changes only became available since the early 2000s. Ocean volume changes induced sea level changes are quantified using ocean temperature and salinity. These oceanic properties have been observed via the Argo floats since 2000, with a near-global coverage (i.e., between 80 °N and 65 °S) established in 2005. Considering that the sea level budget comparison can only be performed over the overlapping period of all available data sets, the attempt to determine the closure of the budget based on observations becomes feasible after 2005. Furthermore, synthesizing measurement on different sea level contributors requires careful investigation to ensure an apple-to-apple comparison among data from various observation systems. We analyzed the closure of global and regional sea level budgets in recent decades with updated observations from GRACE and GRACE-FO, ARGO floats, altimetry, and others and discussed potential sources of imbalance at the basin scale. Future studies should prioritize quantifying contributions and errors from possible deep ocean warming and human impact on land water storage and analyze more detailed temporal evolution from year to year variability. This topic will be discussed in-depth in Chapter 3 and Chapter 4.

Overall, this dissertation project quantifies the global mean and regional sea level changes in the past two to four decades. Specific research objectives are as follows 1) Reconstruct a long-term land-ice mass changes record which combines the strengths of satellite observations and model outputs, 2) Establish an error budget of reconstructed land ice and propagate that error budget into sea level changes 3) Quantifying the regional and global mean sea level patterns caused by different land-ice mass changes sources, 4) Evaluate in detail the

components of sea level rise over the past 15 years from regional to global scales.

Chapter 2

Four Decades of Observation-Based Sea Level Fingerprinting of Land Ice

2.1 Abstract

Observations of regional sea level change constrain models in charge of projecting future sea level rise to guide adaptation and mitigation strategies. Here, we present observation-based constraints on sea level fingerprints from land-ice mass changes over the past four decades (1980-2019) that triple previous observational records based on time-variable Gravity Recovery and Climate Experiment (GRACE) data alone. For the Greenland and Antarctic Ice Sheets, we use an updated reconstruction of the mass budget for the time periods 1972-2019 and 1975-2019, respectively. For the glaciers and ice caps (GIC), we use surface mass balance from the MERRA-2/GEOS5 re-analysis data for 1980-2019 calibrated with GRACE data during the overlapping period 2002-2019. We find a cumulative sea level rise of 53±4 mm from land-ice mass loss from 1980 to 2019. In the world's most vulnerable cities, we find that the GIC, Antarctica, and Greenland contributed almost equally to regional sea level

rise.

2.2 Introduction

Regional sea level rise is an issue of considerable scientific and societal importance [*Oppenheimer et al.*, 2019]. Multiple factors contribute to regional sea level, including thermal expansion of the ocean, changes in liquid water storage on land, melting of the Greenland and Antarctic Ice Sheets and the World's glaciers and ice caps (GIC) into the oceans, and various modes of Earth crust deformation associated with tectonics, adjustments to loading effects, and post-glacial rebound [*Church et al.*, 2011]. Over the past several decades, changes in sea level have been dominated by the ocean thermal expansion and the melting of land ice, with land ice melt progressively becoming the dominant source of sea level rise [*Kopp et al.*, 2014; *Mouginot et al.*, 2019; *Rignot et al.*, 2019; *Zemp et al.*, 2019]. Land ice melt produces a non-uniform sea level change due to self-attraction, loading effects, and rotational feedback [*Farrell and Clark*, 1976]. This non-uniform sea level change is referred to as sea level fingerprint (SLF) [*Plag et al.*, 2001]. In 2000 km from the melting sources, sea level falls in response to a reduced gravity attraction due to ice mass loss. At the same time, the land beneath and surround the melting land ice rises up in reaction to the release of loading. Although the global averaged sea level rises as melting water enters into the ocean, the combined effects from the release of loading and reduced gravitational attraction lead to a sea level decrease in the field near the mass loss location. In the far field, however, sea level rises as ocean mass conserves. Estimates of land-ice SLF are critical for understanding and constraining reconstructions of regional sea level rise [*Milne and Mitrovica*, 1996].

Prior estimates of land-ice SLF used data from the GRACE mission launched in 2002 or synthetic scenarios of ice sheets and glaciers melt [*Riva et al.*, 2010; *Mitrovica et al.*, 2011; *Hsu and Velicogna*, 2017; *Adhikari et al.*, 2019]. A long-term (i.e. multiple decades) SLF

record is required, however, for detecting the signature of land-ice melt in the tide gauge record and for informing numerical models in charge of projections [*Von Schuckmann et al.*, 2016b]. The theory of SLF has been well understood for five decades [*Farrell and Clark*, 1976], nevertheless few direct observations has successfully detect the phenomenon in the far field near tropics due to large noise to signal ratio in the sea level observations [*Hsu and Velicogna*, 2017] . Currently, it remains a challenge to detect the SLF signal in the tide gauge record given large uncertainties in the tide gauge measurements compared to the magnitude of SLF signal. The SLF signal has been detected using ocean bottom pressure (OBP) records in the tropics where the OBP data errors are the smallest [*Hsu and Velicogna*, 2017].

In this study, we calculate the land-ice SLF for the time period 1980-2019, or four decades, using state-of-art reconstructions of ice mass changes in Greenland, Antarctica, and the GIC. We use a combination of GRACE/GRACE-FO satellite observations, multiple other remote sensing data, as well as global and regional climate model outputs to build the land ice mass variation record for the past four decades. We analyze the SLF results at the global average and regional scales to discuss the impact of different land-ice melting sources on regional sea level and their relative contributions to sea level changes between the poles and lower latitude regions over an extensive period of time. We also compare with existing sea level budget studies and independent GIC observations based on geodetic methods to further analyze the contribution of land ice to the total sea level over different time periods.

2.3 Data and Methodology

2.3.1 Ice Sheets Mass Changes and Errors.

2.3.1.1 Mass Budget Method (MBM) Data

We employ half-degree grid annual ice mass changes of the Greenland and Antarctic Ice Sheets derived from the Mass Budget Method (MBM) for the time period 1979-2018 in Antarctica and updated to include the year 2018-2019 [*Rignot et al.*, 2019]; and for the time period 1972-2018 in Greenland updated to include 2019 [*Mouginot et al.*, 2019]. The MBM compares ice discharge at the grounding line (where ice detaches from the bed and becomes afloat in the ocean) with total surface mass balance (SMB) in the interior. SMB is reconstructed from the Institute for Marine and Atmospheric Research Utrecht (IMAU) at Utrecht University's Regional Atmospheric Climate Model (RACMO) 2.3 part 1 (p1) and part 2 (p2) [*Noël et al.*, 2018b; *Van Wessem et al.*, 2018], which is constrained by European Centre for Medium-Range Weather Forecasts (ECMWF) ERA-Interim reanalysis data at the lateral boundaries, with output products at 11 km posting in Greenland and 27 km in Antarctica. RACMO2.3p1 and p2 are available from 1979 to 2019, and 1979 to 2019, respectively. Topography, snow proprieties, and precipitation has been updated in the part 2 version of the model [*Van Wessem et al.*, 2018]. The SMB component of RACMO2.3 is modeled with the dynamics from the High Resolution Limited Area Model (HIRLAM) [*Van de Wal et al.*, 2012; *Van Wessem et al.*, 2014]. SMB is accumulated over 155 major basins in Antarctica and 226 glacier systems in Greenland. Ice discharge is calculated using ice velocity data from MeASUREs [*Rignot et al.*, 2011], ice thickness from BedMachine Greenland version 3.0 [*Morlighem et al.*, 2017] and Antarctica version 1.0 [*Morlighem et al.*, 2020], and grounding line locations and ice front positions derived from differential radar interferometry [*Rignot et al.*, 2011] and optical and radar imagery, respectively. Ice thickness

is adjusted for ice thinning in rapidly evolving basins of Greenland and West Antarctica.

2.3.1.2 Generating Spatial Fields of Ice Sheets Mass Changes

Here, we are interested not only in the ice sheet mass balance but also in the spatial pattern of the mass loss because the SLFs depend on both the magnitude of the mass loss and its geographic distribution. SMB is readily re-sampled on a 0.5 by 0.5 degree grid for compatibility with GRACE/GRACE-FO, but the loss from ice discharge is not naturally gridded since it is calculated at the grounding line. The imbalance in ice discharge - or dynamic thinning - typically spreads inland, as documented for instance by the thinning of glaciers far inland observed using ICESat and ICESat-2 altimetry data (e.g. *Smith et al.* [2020]). We do not have observations of changes in ice velocity and thickness gradients inland of sufficient precision to calculate thinning from ice dynamics on a regular grid. Here, instead we artificially spread the mass loss calculated at the grounding line over a wider area. We evaluate different procedures to spread the loss, including as a function of surface elevation, ice speed, flux density (i.e., the product of thickness and speed), or simply in a uniform fashion. To evaluate the results, we compare the corresponding pattern of mass loss with that retrieved from GRACE/GRACE-FO at a spatial resolution of 300 km near the coast. In the basins of Totten, Moscow, Denman, Getz, and Amery, we previously found that the best match with the GRACE data is obtained when we spread the dynamic loss with the flux density scaled with a power coefficient of 0.6 [*Mohajerani et al.*, 2019]. In this study, we therefore apply the same scaling to all the basins in Antarctica and Greenland.

We calculate the cumulative mass balance, M(t), by adding up monthly mass balance starting at January 1980. Note that the cumulative mass balance does not depend on a reference time period for SMB or ice discharge since the reference mass balance is by definition zero. For each glacier, we calculate the trend in mass balance, dM(t)/dt, as the averaged mass changes over the 40 years (i.e., cumulative mass changes divided by 40 years where the

cumulative mass changes is calculated as the M(t) of the year 2019 subtract that of the year 1980) as in *Rignot et al.* [2019] and *Mouginot et al.* [2019]. The acceleration of ice sheets are obtained by a quadratic regression. A basin contains multiple glaciers and we calculate the trend of the basin as the total cumulative mass changes over the entire basin divided by 40 years. We calculate gridded trends by uniformly spreading the trend of the entire basin within the corresponding grid points of the basin. As for the gridded trend errors, we first compare the trend error to the trend at the basin scale and calculate a ratio as the trend error divided by the trend. Then, at each grid point, we generate a gridded trend error by multiplying the grid cell trend value with the corresponding basin error to trend ratio. We do not attempt to calibrate the MBM results with the GRACE/GRACE-FO data during the overlapping period because the difference between these estimates is small and within errors in Greenland [*Shepherd et al.*, 2020], West Antarctica, and the Antarctica Peninsula [*Shepherd et al.*, 2019]. We note, however, that differences exist in mass balance estimates for East Antarctica that have not been resolved [*Shepherd et al.*, 2019]. Here, we assume that the MBM results, which reveal a state of mass balance in the interior and a state of mass loss in a few coastal regions, are more realistic because the results from altimeters mix radar and laser altimetry data over shorter and disjoint time periods with difficulties to translate volume changes in mass changes in the interior [*Shepherd et al.*, 2020], while the GRACE results in interior East Antarctica are affected by residual uncertainties in GIA correction [*Velicogna et al.*, 2020].

2.3.2 Glaciers and Ice Caps Mass Changes and Errors.

2.3.2.1 GRACE and GRACE-FO data

We focus on 7 regions which dominate the glaciers and ice caps (GIC) mass loss during the GRACE and GRACE-Follow On (GRACE/GRACE-FO) period: 1) Canadian Arctic

Archipelago (CAA), 2) Alaska (ALK), 3) Patagonia North and South Ice Fields (PAG), 4) High Mountains of Asia (HMA), 5) Iceland (ICL), 6) Russian Arctic (RUS), and 7) Svalbard Island (SVL) based on their total contribution to sea level [*Ciracì et al.*, 2020]. Other regions, e.g. New Zealand, the Alps, etc. are excluded from the analysis because their contribution is small and within the noise. We define each GIC region domain based on *Ciracì et al.* [2020]. We calculate GIC monthly mass changes after April 2002 using GRACE/GRACE-FO gravity solutions. We used the GRACE/GRACE-FO spherical harmonic Release-6 (RL06) gravity solutions up to degree and order 60 from the Center for Space Research (CSR) at the University of Texas over the time period April 2002 to September 2019 [*Bettadpur*, 2012; *Tapley et al.*, 2004]. We replace the GRACE/GRACE-FO harmonic coefficients C2,0 (degree 2, order 0) by monthly estimates from the satellite laser ranging (SLR) from Goddard Space Flight Center (GSFC) [*Loomis et al.*, 2019]. C2,0 coefficients use to be calculated with a fixed background model [*Cheng and Ries*, 2017]. *Loomis et al.* [2019] updated the solution by using a time-variable gravity model based on GRACE to derive the C2,0 coefficients in a forward modeling of the SLR solution. We followed a self-consistent geocenter method designed by *Sutterley and Velicogna* [2019] to generate the degree-1 coefficients which are not measured by GRACE. We accounted for the self-attraction and loading effects and the variation of the Earth's geocenter in calculating the degree-1 coefficients. We use coefficients from *Wahr and Zhong* [2013] model forced with ICE-6G loading history to remove signals of the glacier isostatic adjustment (GIA) [*Peltier et al.*, 2015]. GIA is the solid Earth's viscoelastic response to the glacial removal in the last ice age. The GIA phenomena is an ongoing land uplifting and sinking which happens under and around where there were glaciers and ice sheets 16,000 years ago. We also remove the Earth's viscoelastic response to the Little Ice Age (LIA) glacial removal which was not accounted for in the same GIA model. We adopt the post-LIA trend values mainly from *Jacob et al.* [2012] which built a viscoelastic model to derive the upper bounds for LIA trends in GIC regions including Alaska, High Mountains of Asia, and Patagonia North and South Ice Fields. We updated

the LIA trend value in Iceland using the latest results from *Sørensen et al.* [2017]. Correcting trends associated with the LIA is an unique and essential procedure for reconstructing mass changes over the GIC regions, given the fact that a lack of consideration of the LIA-induced gravity trend would lead to an underestimate of the contemporary ice mass loss in GIC regions [*Jacob et al.*, 2012]. We substitute the GRACE/GRACE-FO C3,0 coefficients with coefficients derived from SLR from GSFC [*Loomis et al.*, 2019]. GRACE/GRACE-FO C3,0 coefficients are of lower quality due to the lack of an accelerometer onboard of GRACE and also an anomaly in the one of the two accelerometers onboard of GRACE-FO [*Velicogna et al.*, 2020].

2.3.2.2 Least Squares Fit Mascon Approach

We calculate GIC mass changes time series from the GRACE/GRACE-FO spherical harmonics using a least squares fit mascon approach [*Ciracì et al.*, 2020; *Jacob et al.*, 2012]. We use mass concentration blocks (mascon) to cover GIC regions that have areas greater than 100 square km as defined by the latest version of the Randolph Glacier Inventory [*Pfeffer et al.*, 2014], Version 6.0, (RGIv6) . Each mascon is composed of several 0.5 by 0.5 degree latitude-longitude grid cells. We arrange the grid cells within each mason and the arrangement of mascons with respective to each other following *Ciracì et al.* [2020]. *Ciracì et al.* [2020]'s mascon configuration maximizes the signal to noise ratio when retrieving GIC signals from the satellite gravimetry observations. The optimal arrangement is chosen based on the ability to retrieve the signal inside of the target mascon and at the same time to minimize the signal from outside that leaked into the target mascon through some inevitable procedures to convert the GRACE/GRACE-FO stokes coefficient into spatial fields. More specifically, potential causes for signal leakage include the truncation of GRACE/GRACE-FO spherical harmonics and the assumption of a uniform mass distribution within each mascon [*Jacob et al.*, 2012; *Velicogna and Wahr*, 2013]. To reduce signal leakage, we place mascons to cover

the plains of Northern India, Pakistan, and Bangladesh in order to prevent signals leaked from the local groundwater extractions in these region [*Rodell et al.*, 2009; *Tiwari et al.*, 2009]. In addition, we also cover the Greenland and Antarctica with mascons to account for a lack of realistic hydrological solutions on both ice sheets. We do not, however, cover the entire globe with mascons, to avoid higher noise level associated with the increased number of mascons [*Jacob et al.*, 2012; *Tiwari et al.*, 2009]. To retrieve mass changes signals from mascons, we calculate a set of stokes coefficients up to degree 60 for each mascon. The stokes coefficients are converted to mass and smoothed with a 150 km Gaussian function [*Ciracì et al.*, 2020]. Then for each mascon, we obtain its monthly mass changes by fitting the stokes coefficients to the monthly GIA and hydrology-corrected GRACE/GRACE-FO stokes coefficients. Finally, the regional mass changes time series for each glacier is calculated as the sum of total mass changes of all the mascons within the glacier region, and the mass changes time series within each mascon is the same on each grid point based on a uniform mass distribution assumption.

2.3.2.3 Surface Mass Balance from Regional and Global Climate Models

To bridge the gap, from July 2017 to May 2018, which is between the GRACE and GRACE-FO missions, we use SMB monthly output products from Modern-Era Retrospective analysis for Research and Applications version 2 (MERRA-2). MERRA-2 is the NASA's GMAO latest atmospheric reanalysis since the 1990s [*Gelaro et al.*, 2017]. The GEOS version 5.12.4 is used in the MERRA-2 to assimilate the atmospheric data. MERRA-2 take the place of its predecessor, MERRA, by fixing a number of biases in the original model [*Rienecker et al.*, 2011]. For instance, MERRA-2 corrects non-physical jumps and artificial precipitation trends induced by the changes in the observation system [*Gelaro et al.*, 2017]. Some atmospheric and land surface hydrological properties also achieve balance in the new model. Furthermore, MERRA-2 has more accurate representation of the upper stratosphere and assimilates state-

of-art satellite measurements. The latest GEOS version 5.12.4 prescribes more precise snow processes with improved algorithm of albedo, refreezing, snow melt runoff, densification, and percolation. Moreover, it increases the ice column to 15 layers to allow a more realistic simulation of heat exchange between snow and ice [*De Woul and Hock*, 2005]. MERRA-2 has SMB products for most of the world's glaciers and ice caps, including the seven major GIC in our studies, plus Central Europe and New Zealand. As the we define the GIC regions following glacier domains in the RGIv6 [*Pfeffer et al.*, 2014], we created glaciers masks for some modeled glacier domains if the area covered with land ice exceeds two times of the area defined in the RGIv6. These ad hoc masks were applied to Baffin Island (i.e., southern part of the Canadian Arctic Archipelago), Iceland, and Novaya Zemlya and Severnaya Zemlya (i.e., two islands of the Russian Arctic).

We process the SMB data following *Ciracì et al.* [2020], *Velicogna et al.* [2014], and *Sutterley et al.* [2014]. We define the SMB as the net balance between accumulation from precipitation, evaporation and the ablation from runoff. We neglect the marginal impacts on the GIC mass balance from sublimation and wind erosion. We calculate the cumulative SMB by adding up SMB along time. The cumulative SMB time series match well the GRACE/GRACE-FO time series in terms of seasonal and inter-annual variabilities, but their trends in mass loss, dM/dt, differ (Table 2.1, Figure 2.1). This difference results from factors including: 1) a bias in the absolute SMB in the SMB models, either from excess precipitation or excess surface melt or a combination of both; or 2) a bias caused by ice dynamics in regions with marine- or lake-terminating glaciers, i.e. where the mass balance includes an ice discharge component that the SMB models do not represent. The offset associated with glacier discharge should be small in most GIC regions, except perhaps in Svalbard Island [*Noël et al.*, 2020] and Patagonia North and South Ice Fields [*Mouginot and Rignot*, 2015]; elsewhere, the mass balance signal is dominated by SMB [*Larsen et al.*, 2015; *Millan et al.*, 2017]. We assume that the largest error in M(t) is the reference SMB. For land-terminating glaciers in a state of mass equilibrium, the reference SMB should be zero for that time period, but we are not

sure when these glacier systems were in a state of mass balance. A bias in reference SMB translates into a linear trend in cumulative mass loss M(t). Similarly, a bias introduced by a non-zero ice discharge translates into a linear trend in M(t).

Table 2.1: The overlapping periods between the regional and global climate models with GRACE/GRACE-FO in 7 major GIC regions. Time period starts in April 2002 and ends in December of the corresponding year.

GIC region	Model	Time period
ALK	MERRA-2	2002-2019
CAA	MERRA-2	2002-2019
	RACMO2.3	2002-2015
	MAR3.6	2002-2015
HMA	MERRA-2	2002-2019
	GloGEM	2002-2012
ICL	MERRA-2	2002-2019
	RACMO2.3	2002-2015
	MAR3.6	2002-2015
PAG	MERRA-2	2002-2019
	RACMO2.3	2002-2012
RUS	MERRA-2	2002-2019
	MAR3.6	2002-2015
SVL	MERRA-2	2002-2019
	RACMO2.3	2002-2015
	MAR3.6	2002-2015

2.3.2.4 Surface Mass Balance Bias Correction and Extended GIC Time Series

To correct for this absolute offset in dM/dt in each GIC region, we adjust the 40-year trend of the cumulative anomalies in SMB to match the GRACE/GRACE-FO time series of M(t) during the overlapping period (Figure 2.1, Table 2.1). The model trend offset is calculated as the trend of GRACE/GRACE-FO mass anomalies minus the trend of the cumulative SMB from climate models in their overlapping time periods. Figure 2.1 compares the trend offset in each GIC region with all available regional and global climate models. The models and GRACE/GRACE-FO overlapping periods vary with model lengths as documented in Table

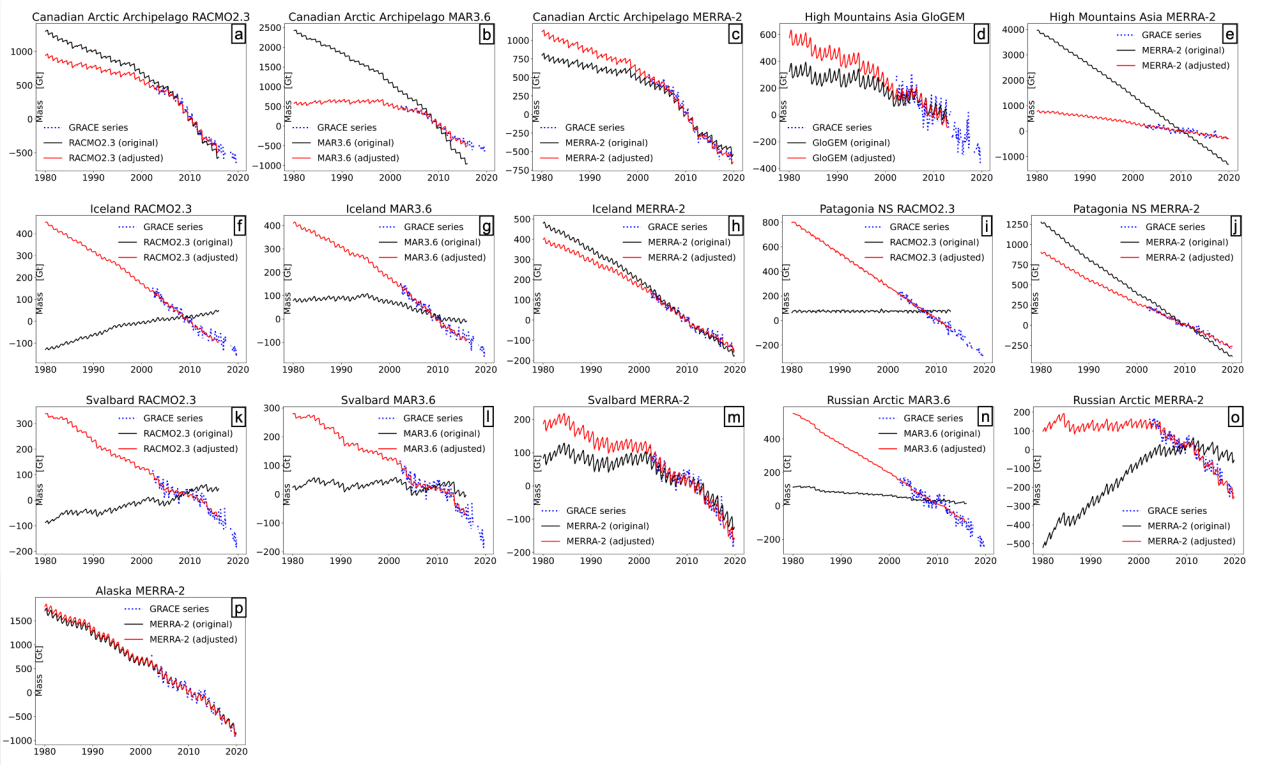

Figure 2.1: Trend adjustment of cumulative surface mass balance (SMB) model time series in seven major GIC regions. The original cumulative SMB time series are in black, and GRACE/GRACE-FO-calibrated time series of modeled SMB are in red. GRACE/GRACE-FO time series are in blue. All available regional and global climate models are shown on the figure, with MERRA-2 being selected for the final SLF reconstruction. Trend differences are calculated over each model and GRACE/GRACE-FO common time periods as in Table 2.1.

2.1 with a time period from April 2002 to December 2015 for most study regions. The trend offset is calculated in the overlapping periods whereas the the offset value is then added to the overall 40-year trend to correct the bias in the modeled cumulative SMB. The trend correction is equivalent to resolving a bias in mean SMB and/or a bias in mean ice discharge if marine-terminating glaciers are present.

After the trend correction, in each GIC region, we concatenate the GRACE-calibrated cumulative SMB from January 1980 to March 2002 with the GRACE/GRACE-FO mass change from April 2002 to September 2019 into a consistent 40-year record. For extended time series in each GIC region, including the two islands of Canadian Arctic Archipelago, we estimate

a trend and an acceleration by simultaneously fitting a trend, acceleration, constant, annual, and semiannual signals to the monthly time series following the regression approach in *Velicogna* [2009].

To generate annual time seris, we select M(t) at June of each year for annual cumulative mass anomalies, as in [*Rignot et al.*, 2019] and [*Mouginot et al.*, 2019], after applying a 13-month smoothing average [*Velicogna*, 2009] to the monthly time series. To obtain gridded mass changes, for each GIC region, we map annual mass changes on a 0.5 by 0.5 degree grid where we uniformly distribute the signal to the grid cells within each GIC region. We also test another distribution approach by uniformly spread the signal within each mascon which maximize the spatial variability of the ice mass changes signal but does not add much spatial details to corresponding SLF pattern at the expanse of higher noise level. As a result, we only generate uniformly distributed ice mass changes within each GIC region for the input fields of SLF.

2.3.2.5 Error Estimates of the Extended GIC time series

We define the trend error as the sum in quadrature of uncertainties in GIA, LIA, mascon least squares fitting, hydrology correction, and statistically error. The GIA and LIA uncertainties are assumed to be the same of the signal's magnitude following *Jacob et al.* [2012]. Two land hydrology models, Community Land Surface Model version 4.5 (CLM 4.5) [*Oleson et al.*, 2010] and Global Land Data Assimilation System 2 (GLDAS 2) [*Roca et al.*, 2009], are used to remove signals leaked from regions surrounding GIC where terrestrial water signals are obvious. The associated hydrology correction error is defined as the difference in the trend of two hydrology models following *Jacob et al.* [2012] and *Ciracì et al.* [2020]. The mascon fitting error is caused by the assumption that mass distributes uniformly in each mascon. We estimate the mascon fitting error using a Monte Carlo approach. In each mascon, we generate 10,000 pseudo solutions from a Gaussian distribution with a zero mean and one standard

deviation as the mass signal of the mascon. We applied least squared fit mascon conversion to these mascons and calculate the time series. We compare 10,000 sets of time series obtained from the uniform distribution assumption and from the random distribution and define the mascon fitting error as the double of the standard deviation of the differences of the 10,000 pairs of time series. The acceleration error accounts for the statistical uncertainty.

To evaluate the impact of climate model selections on the resulting extended GIC time series, we repeat the experiment with MERRA-2 only and then with other global and regional climate models (Table 2.1), including RACMO2.3, Modele Atmospherique Regional3.6 (MAR3.6) [*Fettweis et al.*, 2017], and Global Glacier Model (GloGEM) [*Huss and Hock*, 2015]. The goodness of fit, i.e. root mean square error (RMS), of the calibrated SMB data versus the GRACE/GRACE-FO data during the overlapping period quantifies the SMB error. We further quantify the impact of the model selection on four variables: 1) trend correction values; 2) RMS between model and GRACE/GRACE-FO; 3) 40-year ice mass trend, dM/dt; and 4) 40-year cumulative mass change, $M(2019) - M(1980)$.

After calibration, we find that MERRA-2 has one of the smallest RMS error for the seven regions (Table 2.2). We compare between the RMS of model vs GRACE data with the standard deviation of GRACE/GRACE-FO during the overlapping periods. We also estimate the impact of the model selection on the 40-year trend (Table 2.3) and 40-year cumulative loss (Table 2.4). In 2.3 for each region, we estimate the uncertainty as the standard deviation between the 40-year trends estimated from extended time series reconstructed using different models. For each extended GIC time series, we estimate its trend by simultaneously fitting a trend, acceleration, constant, annual, and semiannual signals to the monthly time series. The trend error is the sum in quadrature of uncertainties in GIA, LIA, mascon fitting error, hydrology correction error, and the statistical error. We define the percentage error as the standard deviation error divided by the MERRA-2 trend estimates in corresponding regions. For Alaska, we have only one model available, so we use the error for the other 6 regions

combined together as a proxy for Alaska. We estimate it from the mean error of the other regions, which is 8%, or 5.4 Gt/yr. We first calculate the percentage error for Alaska as the sum in quadrature of errors in other 6 regions divided by the total trend of the 6 regions estimated based on MERRA-2. Overall, the uncertainty in trend for the seven regions is 12.1 Gt/yr, or 6% of the signal. The cumulative error for the 7 regions is 521 Gt, or 6.5% of the signal. We use this error based on the model selection to quantify the error in GIC estimate, i.e. we assume a 6.5% error in trend and cumulative loss of the GIC over the last 40 years.

	ALK	CAA	HMA	ICL	PAG	RUS	SVL
Models	MERRA-2	MERRA-2	MERRA-2	MERRA-2	MERRA-2	MERRA-2	MERRA-2
	-	RACMO2.3	-	RACMO2.3	RACMO2.3	-	RACMO2.3
	-	MAR3.6	-	MAR3.6	-	MAR3.6	MAR3.6
	-	-	GloGEM	-	-	-	-
RMS model vs GRACE	28.6	22	32.1	5.9	6.4	11.5	9.6
	-	19.5	-	5.5	9	-	7.6
	-	22.4	-	5.2	-	15.2	7.1
	-	-	35.3	-	-	-	-
σ GRACE [Gt]	318	367	128	74	128	88	53
	-	1279	-	61	69	-	32
	-	280	-	65	-	61	32
	-	-	74	-	-	-	-
RMS/σ	9%	6%	25%	8%	5%	13%	18%
	-	7%	-	9%	13%	-	24%
	-	8%	-	8%	-	25%	22%
	-	-	48%	-	-	-	-

Table 2.2: Comparison between the root mean square error (RMS) of model vs GRACE/GRACE-FO data with the standard deviation of GRACE during the overlapping periods. The second row 'RMS model vs. GRACE [Gt]' is the RMS between the modeled cumulative SMB and GRACE/GRACE-FO mass changes. The RMS is calculated after the trend corrections being applied on the cumulative SMB. The RMS indicates the goodness of the fit of the calibrated SMB data versus the GRACE/GRACE-FO data during their overlapping periods and is also used to quantify the monthly errors of cumulative SMB time series. The third row 'σ GRACE [Gt]' is the standard deviation of GRACE/GRACE-FO time series. The last row 'RMS/σ' compares the monthly variability of the cumulative SMB with that of the GRACE/GRACE-FO time series. Overall, MERRA-2 has the smallest RMS to σ ratio in all 7 study regions.

	ALK	CAA	HMA	ICL	PAG	RUS	SVL
Models	MERRA-2	MERRA-2	MERRA-2	MERRA-2	MERRA-2	MERRA-2	MERRA-2
	-	RACMO2.3	-	RACMO2.3	RACMO2.3	-	RACMO2.3
	-	MAR3.6	-	MAR3.6	-	MAR3.6	MAR3.6
	-	-	GloGEM	-	-	-	-
dM/dt [Gt/yr]	-68±6	-45±8	-27±5	-14±3	-30±5	-9±3	-9±1
	-	-41±8	-	-15±3	-27±5	-	-13±1
	-	-32±8	-	-14±3	-	-19±3	-12±1
	-	-	-22±5	-	-	-	-
Error [Gt/yr]	**5.4**	6.7	3.5	0.6	2.1	7.1	2.1
Error [%]	**8%**	15%	13%	4%	7%	79%	23%

Table 2.3: Uncertainties in 40-year trend associated with SMB model selection. In each region, we estimate the uncertainty as the standard deviation between the 40-year trends estimated from extended time series reconstructed using different models. For each extended GIC time series, we estimate its trend by simultaneously fitting a trend, acceleration, constant, annual, and semiannual signals to the monthly time series. The trend error is the sum in quadrature of uncertainties in GIA, LIA, mascon fitting error, hydrology correction error, and the statistical error. We define the percentage error as the standard deviation error divided by the MERRA-2 trend estimates in corresponding regions. For Alaska, we have only one estimate from MERRA-2, so the error is unknown. We estimate it from the mean error of the other regions, which is 8%, or 5.4 Gt/yr. We first calculate the percentage error for Alaska as the sum in quadrature of errors in other 6 regions divided by the total trend of the 6 regions estimated based on MERRA-2. The error of Alaska is The total mass loss from MERRA-2 is 202 Gt versus a total error of 12.1 Gt, or 6%.

2.3.2.6 Sea Level Fingerprints and Errors

We combine the above-calculated ice sheets and GIC mass changes as loading fields and solve for the SLF using a pseudo-spectral approach [*Mitrovica et al.*, 2001; *Hsu and Velicogna*, 2017]. We use a simple regression to estimate trend, acceleration and the cumulative change in SLF. We calculate SLF trend errors with the following procedure. First, we combine ice sheets and GIC trend errors onto a global half degree grid. Then, on each grid cell, we use a Monte Carlo simulation to generate 1,000 values following a Gaussian pseudo-random distribution with a standard deviation equal to the trend error. After that, on each grid cell, we calculate 1,000 SLF. Finally, the SLF trend error (1 σ) at each grid cell is calculated as the standard deviation of 1,000 SLF values. We calculate the SLF cumulative change error following the same procedure. We test distribution of the output 1,000 simulations of SLF

	ALK	CAA	HMA	ICL	PAG	RUS	SVL
Models	MERRA-2	MERRA-2	MERRA-2	MERRA-2	MERRA-2	MERRA-2	MERRA-2
	-	RACMO2.3	-	RACMO2.3	RACMO2.3	-	RACMO2.3
	-	MAR3.6	-	MAR3.6	-	MAR3.6	MAR3.6
	-	-	GloGEM	-	-	-	-
M(t) [Gt]	-2689±68	-1788±43	-1056±112	-559±13	-1186±24	-347±36	-372±18
	-	-1614±38	-	-611±14	-1081±27	-	-524±16
	-	-1247±42	-	-570±13	-	-802±37	-465±15
	-	-	-854±107	-	-	-	-
Error [Gt]	**242**	276	143	27	74	322	77
Error [%]	**9%**	15%	14%	5%	6%	93%	21%

Table 2.4: Uncertainties in 40-year cumulative mass changes associated with SMB model selection. In each region, we estimate the uncertainty as the standard deviation between the 40-year cumulative mass changes estimated from extended time series reconstructed using different models. Cumulative mass change is calculated as the mass anomaly at 2019 minus the that of 1980. Cumulative mass changes error is calculated as the sum of quadrature of the monthly errors of the first and last month of the 40-year time period. During the GRACE/GRACE-FO period, the monthly errors are GRACE/GRACE-FO monthly errors [*Wahr et al.*, 2006]. For time periods beyond the GRACE/GRACE-FO periods, the monthly errors are RMS btween trend-adjusted cumulative SMB and GRACE/GRACE-FO. We then calculate the percentage error by dividing by the MERRA-2 estimate. For Alaska, we have only one estimate, so the error is unknown. We estimate it from the mean error of the other regions, which is 461 Gt for a total loss of 5,308 Gt, or 9%; which translates into an error of 242 Gt for Alaska. The total mass loss from MERRA-2 is 7,998 Gt with an error of 521 Gt, or 6.5%.

trend fields and find it nearly follows the a Gaussian distribution as in Figure 2.4, which gives us confidence in our Monte Carlo approach. Figure 2.2 shows the trend error map of 40-year SLF from total land ice uncertainties. SLF trend errors correspond to the input mass errors loading field (Figure 2.3), where ice sheets have the largest uncertainty.

2.4 Results

Over the last 40 years, the world's GIC experienced a mass loss that averaged 202±13 Gt/yr (gigaton = 10^{12} kg) (Figure 2.5) with an acceleration of 4.6±0.2 Gt per year squared, for a cumulative mass loss of 7,998±520 Gt. 72% of the GIC mass loss is from the 5 arctic regions, with Alaska alone contributing 34% of the signal (Figure **??**). We find a significant

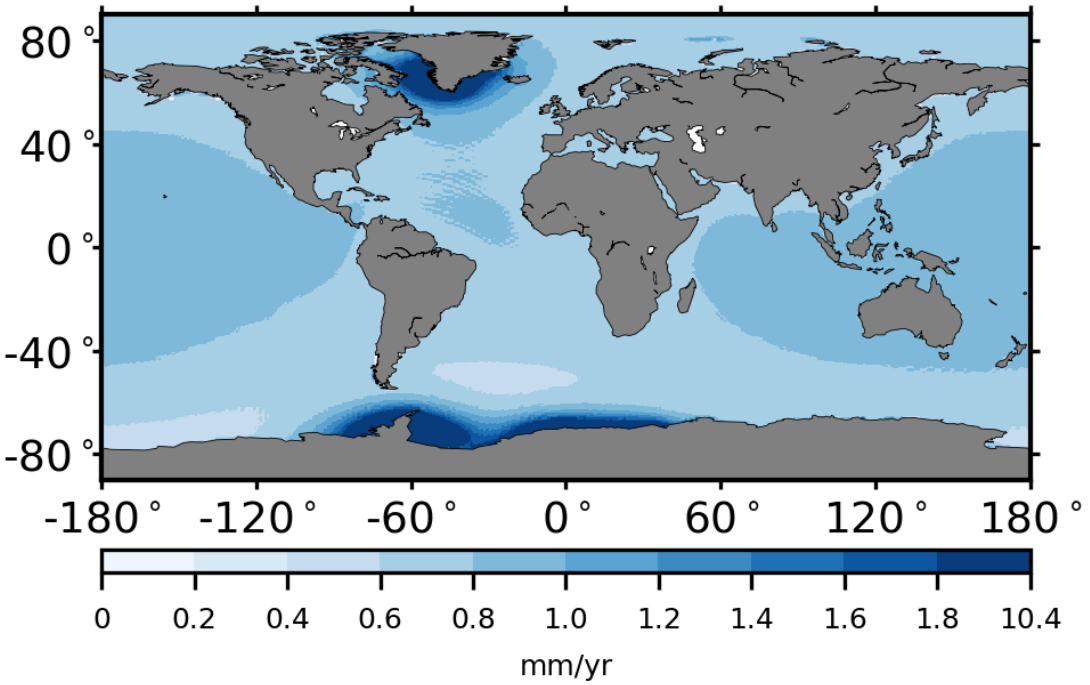

Figure 2.2: SLF trend error due to land ice mass uncertainties over 1980-2019. We calculate SLF trend errors with the following procedure. First, we combine ice sheets and GIC trend errors onto a global half degree grid. Then, on each grid cell, we use a Monte Carlo simulation to generate 1,000 values following a Gaussian pseudo-random distribution with a standard deviation equal to the trend error. After that, on each grid cell, we calculate 1,000 SLF. Finally, the SLF trend error (1 σ) at each grid cell is calculated as the standard deviation of 1,000 SLF values.

acceleration in mass loss in Canadian Arctic Archipelago since the late 1990s, which has been attributed to increasing summer air temperature caused by negative North Atlantic Oscillations [*Noël et al.*, 2018a].

For Greenland, the mass loss averaged 143±10 Gt/yr over the last 40 years, with an acceleration of 9.4±0.4 Gt per year squared (Figure 2.7). In total, Greenland contributed 5,648±400 Gt of mass loss to the ocean, i.e. less than the GIC. In the last 20 years, however, the mass loss from the Greenland Ice Sheet increased faster, at a rate of 254±25 Gt per year, or twice the average rate for the last 40 years.

For Antarctica, the contribution to sea level rise over the entire period is nearly the same as

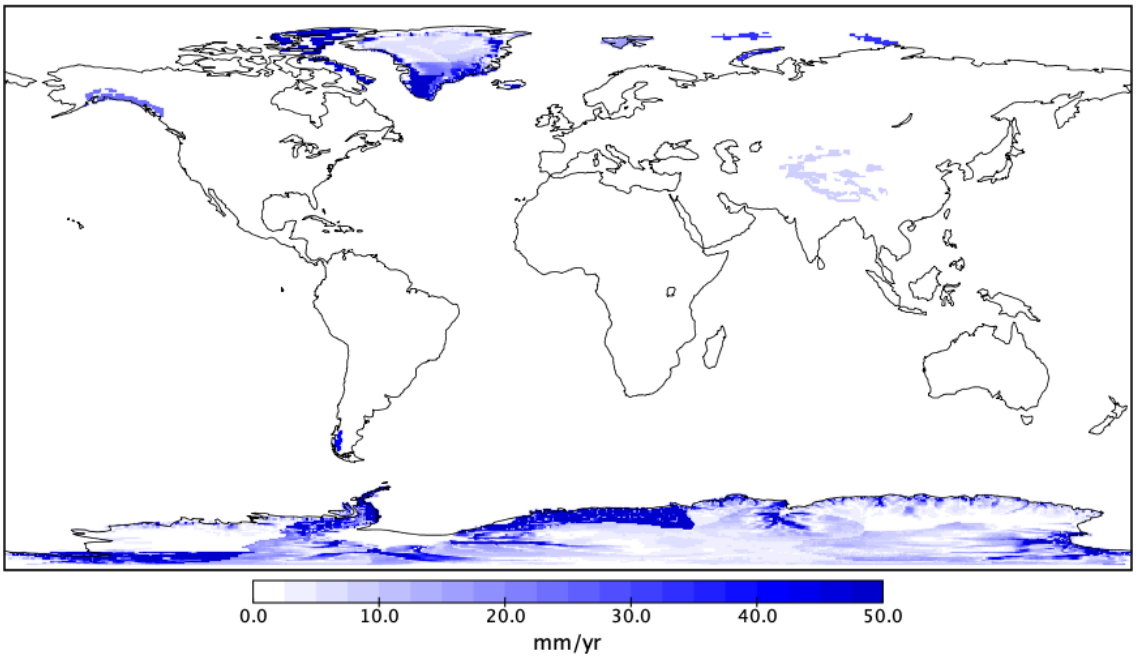

Figure 2.3: Trend error of land ice mass uncertainties in cm water equivalent over 1980-2019. This spatial field of land ice trend errors is used for the input to calculate the associated trend error of SLF over 1980-2019

for Greenland, with 5,383±1245 Gt of mass loss, or an average 136±31 Gt/yr and an acceleration of 8±1 Gt per year squared (Figure 2.7). The reason for the high total cumulative loss from Antarctica is that the continent was in a state of negative mass balance almost the entire time period whereas the Greenland Ice Sheet was nearly in a state of net mass balance from 1979 to the early 1990s. The mass loss also increased more slowly in Antarctica than in Greenland in the 1990s. We have no independent estimate of mass loss in East Antarctica for the early period 1980-1990s, but its state of mass loss is consistent with an ice front retreat in the Wilkes Land sector of East Antarctica [*Miles et al.*, 2018] and the disappearance of several ice shelves [*Frezzotti et al.*, 1998; *Rignot et al.*, 2019].

Comparing the GIC and ice sheets over the first twenty years (1980-1999), the GIC contributed 3,014±370 Gt of mass loss versus 712±282 Gt for Greenland and 1,128±891 Gt for Antarctica, i.e. GIC was dominant. In the 1990s and 2000s, however, the ice sheet mass

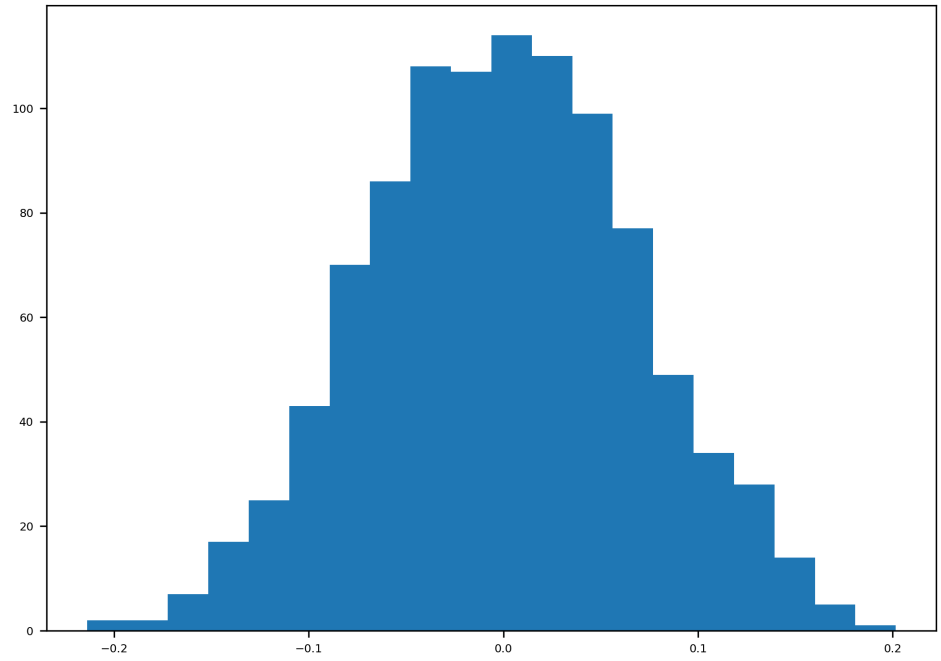

Figure 2.4: Distribution of 1,000 SLF trend simulations.

loss accelerated markedly and eventually exceeded that of the GIC (Figure **??**). We estimate that the crossing point where GIC and ice sheet losses were nearly equivalent occurred around year 2008. After 2008, the acceleration in ice sheet mass loss remained systematically larger than for GIC, hence the ice sheet mass loss became increasingly larger than that of the GIC. As the ice sheets contain a much larger ice volume that the GIC (or two orders of magnitude), and because enhanced surface melt will continue in Greenland and the GIC [*Hamlington et al.*, 2020], and warmer ocean temperatures will continue eroding ice and destabilize glaciers at the margins of Greenland and Antarctica [*Joughin et al.*, 2014; *Catania et al.*, 2018], the dominance of the ice sheet loss over the GIC is expected to persist and even increase in the coming decades.

Combining the GIC and ice sheets, we calculate a cumulative ice mass loss of 19,029±1,407 Gt for 1980-2019, or 481±36 Gt/yr, or 53±4 mm of sea level, or an average 1.33±0.1 mm/yr

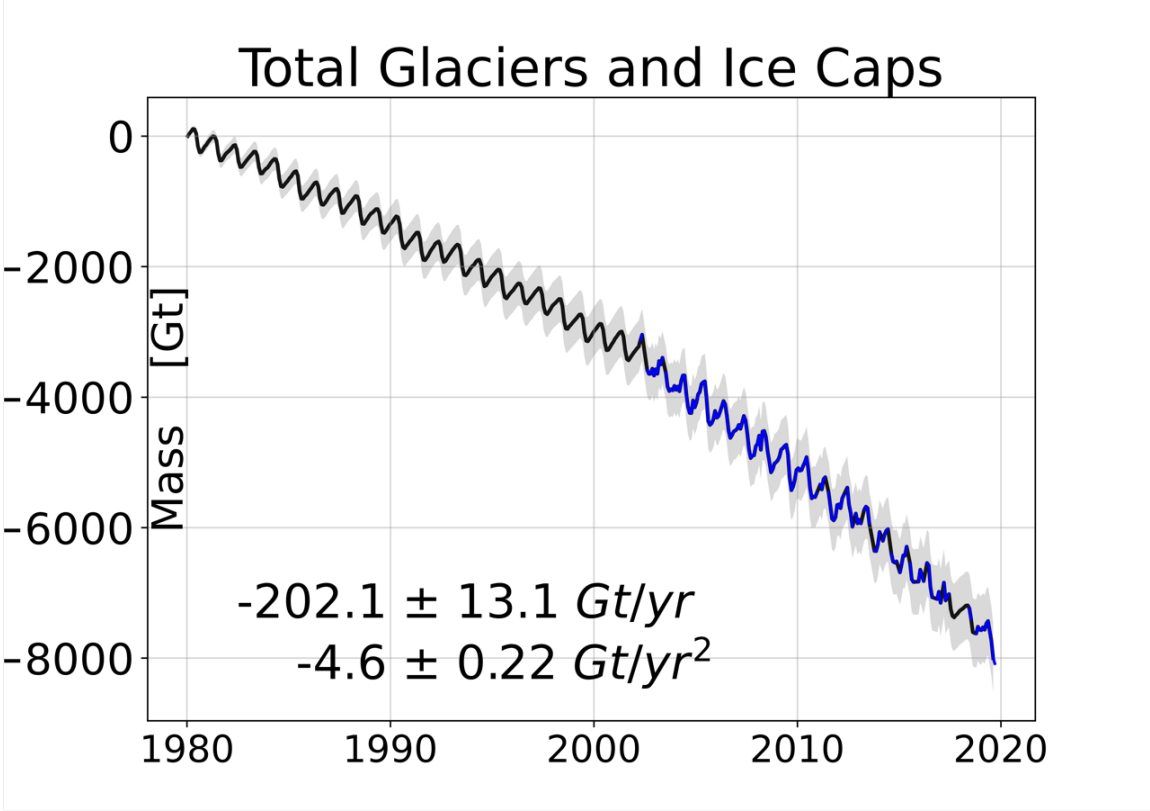

Figure 2.5: 40-year time series of total mass anomaly from seven Glacier and Ice Caps (GIC) regions. Grey shades indicate error band at 68% confidence level. The GIC time series include 2 sections: 1) Pre-GRACE January 1980 to March 2002 (black) and GRACE/GRACE-FO gap January 2017 to December 2018 (black), and 2) GRACE/GRACE-FO April 2002 to present (blue) with a gap in between. Over the GRACE/GRACE-FO period, the monthly error is calculated as the GRACE/GRACE-FO monthly errors. Beyond the GRACE/GRACE-FO period, the monthly error is calculated as the RMS between trend corrected modeled cumulative SMB and GRACE/GRACE-FO time series during their overlapping periods.

of sea level rise. In terms of SLF (Figure 2.9d), sea level rise exceeds 53 mm along a wide tropical to sub-tropical band between -40° and +40° latitude. The SLF is negative (i.e. sea level lowering) near the sources of mass loss around the ice sheets due to reduced gravitational attraction from the land-ice. The largest rate of sea level lowering is recorded along West Greenland. The largest rates of sea level rise are recorded in the tropical Pacific ocean. Comparing the SLF from the GIC, Greenland and Antarctica, the spatial pattern exhibits the largest differences nearest to the sources of the mass loss (Figure 2.9), as expected.

The evolution of the ice sheet loss is reflected in the SLFs in two ways (Figure 2.10). First,

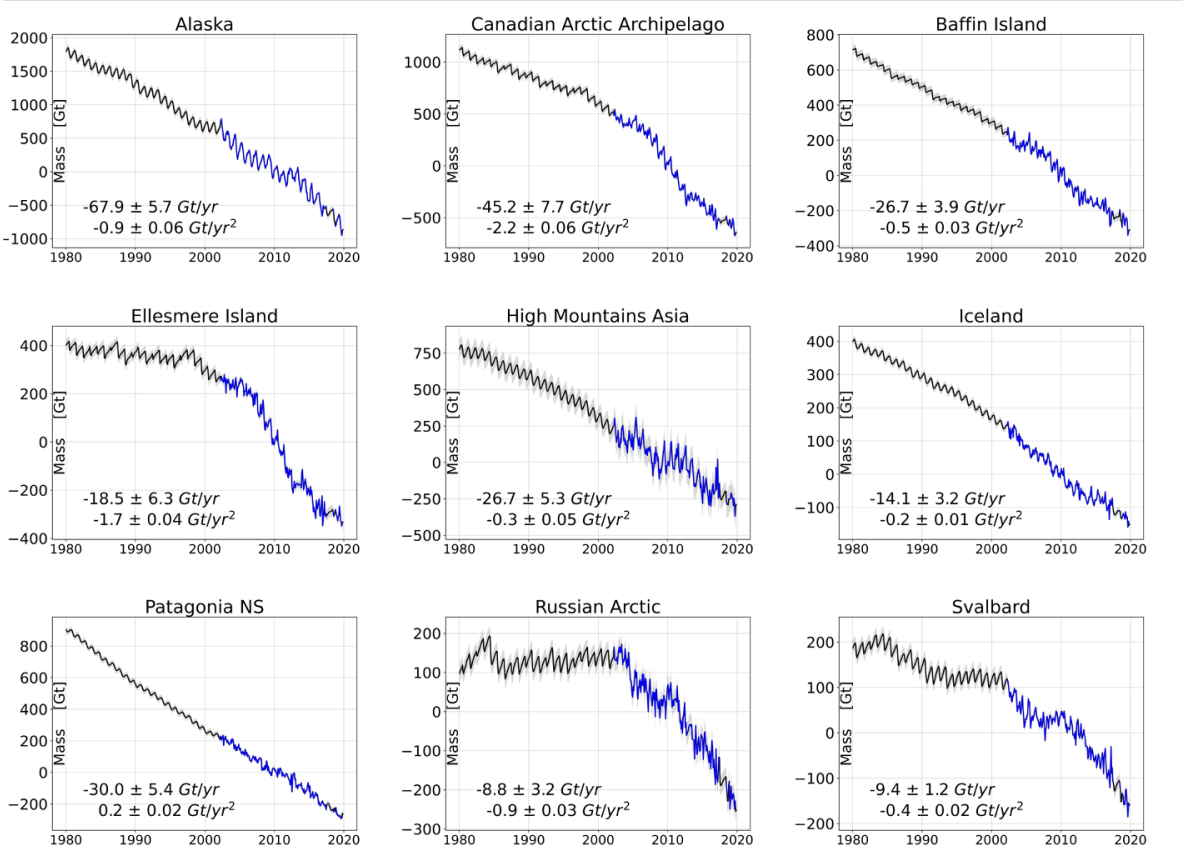

Figure 2.6: 40-year time series of Glacier and Ice Caps (GIC) regions. The GIC time series include 2 sections: 1) Pre-GRACE January 1980 to March 2002 (black) and GRACE/GRACE-FO gap January 2017 to December 2018 (black), and 2) GRACE/GRACE-FO April 2002 to present (blue) with a gap in between. For each extended GIC time series, we estimate its trend and acceleration by simultaneously fitting a trend, acceleration, constant, annual, and semiannual signals to the monthly time series. The trend error is the sum in quadrature of uncertainties in GIA, LIA, mascon least squares fitting, hydrology correction, and statistically error. The acceleration error accounts or the statistical uncertainty.

the rate of sea level change increased markedly from the first 20 years (1980-1999) to the last 20 years (2000-2019). The barystatic equivalent trends are 0.67 mm/yr and 2.00 mm/yr, respectively, i.e. a factor 3. Second, the more rapid increase in SLF in 2000-2019 is concentrated in the tropical band.

To examine the record at the regional level in detail, we analyze the SLF for major coastal cities that have been identified by various studies as most at risk of exposure to sea level rise, with high economical and human impacts. Most of these cities have population greater than

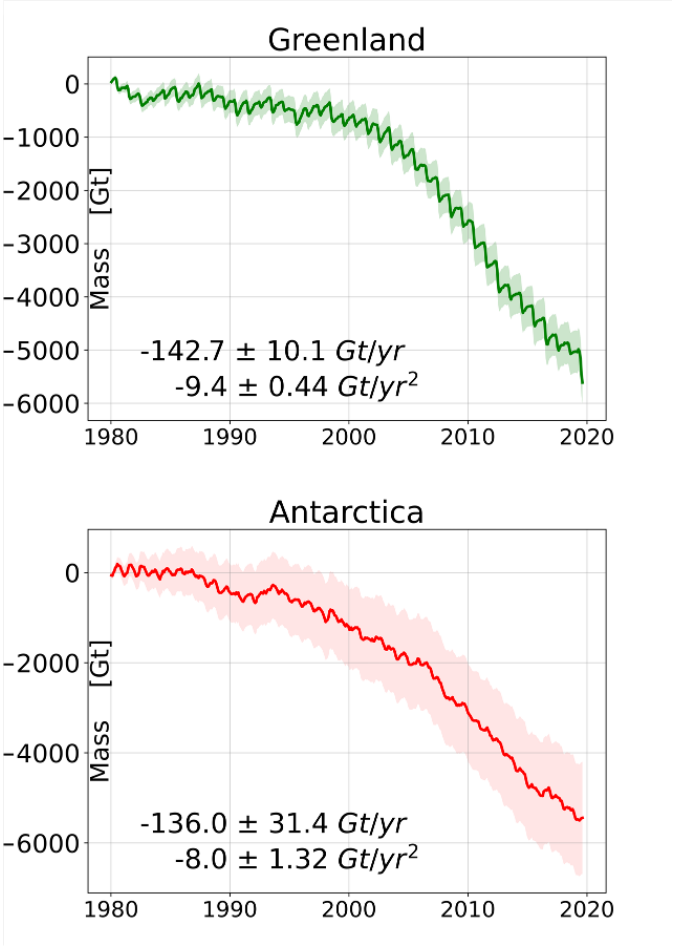

Figure 2.7: 40-year time series of the ice mass balance of Greenland and Antarctica. Ice sheets time series and associated monthly errors are extended from *Rignot et al.* [2019] and *Mouginot et al.* [2019]. The trends of ice sheets are defined as the averaged mass changes over the 40 years, i.e., the cumulative mass changes divided by 40 years, as in *Rignot et al.* [2019] and *Mouginot et al.* [2019]. The acceleration of ice sheets are obtained by a quadratic regression.

10 million people. The cumulative sea level rise is 2-to 8% above the global mean (53 mm) in many of these major coastal cities (Figure 2.11), e.g. Jakarta, Durban, Manila, Tokyo, Lima, Lagos, Bangkok, Shanghai, Rio de Janeiro, and Melbourne, because they are in the far field of the strongest land-ice mass loss signals from Greenland, Western Antarctica, Alaska, and Canadian Arctic Archipelago. The GIC contributes the most cumulative SLF change in the aforementioned cities. When we combine the effect of the Greenland and Antarctic ice sheets, we find that the ice sheets produced the largest contribution to SLF in all the selected

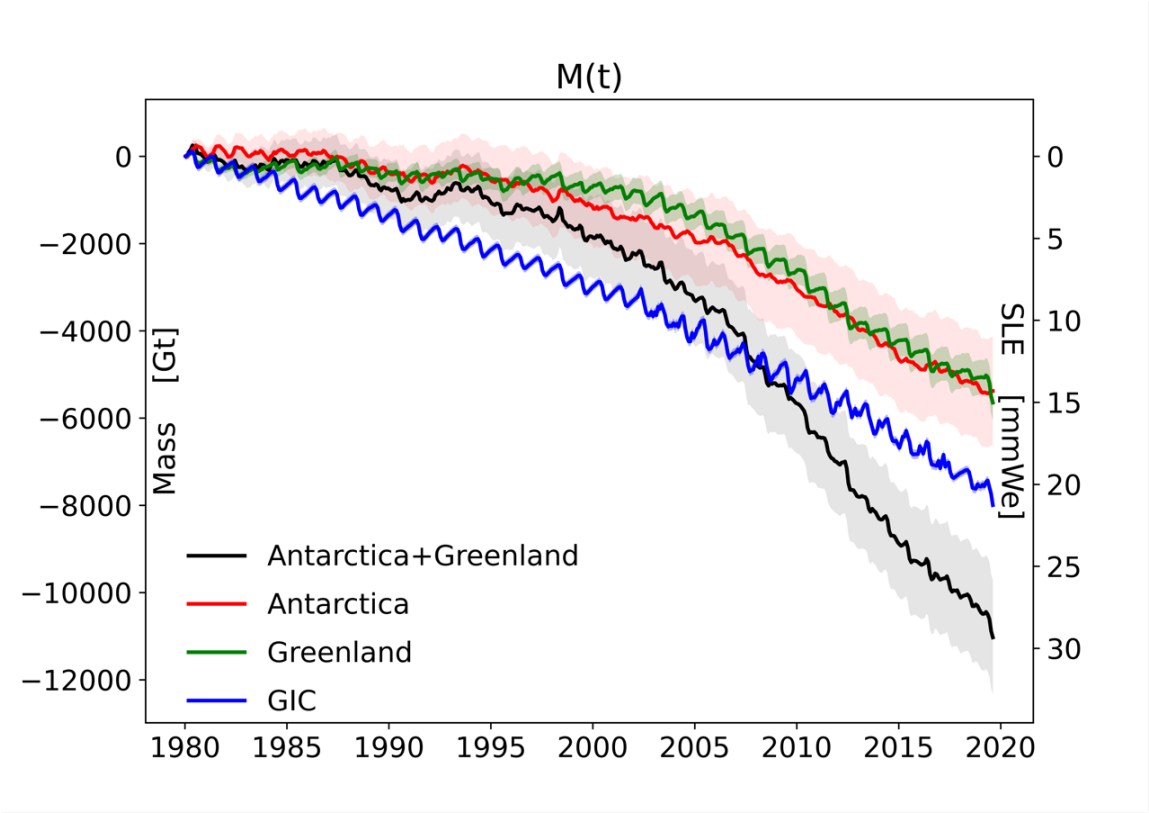

Figure 2.8: Comparison of 40-year time series of the ice mass balance of GIC, Greenland and Antarctica ice sheets. GIC was dominant in the first twenty years (1980-1999). In the 1990s and 2000s, however, the ice sheet mass loss accelerated markedly and eventually exceeded that of the GIC. We estimate that the crossing point where GIC and ice sheet losses were nearly equivalent occurred around year 2008. After 2008, the acceleration in ice sheet mass loss remained systematically larger than for GIC, hence the ice sheet mass loss became increasingly larger than that of the GIC.

cities over the past four decades. Despite being the most remote from local populations, the ice sheets are the most relevant to sea level rise affecting densely populated areas. While slight differences exist in the partitioning of the SLF in these cities between Greenland, Antarctica, and the GIC, however, we find that over the entire time period of 1980-2019 the three components have contributed nearly equally to the total SLF. The dominant pattern of SLF is higher in the tropical to sub-tropical band between -40° and +40° but favorably lower at higher latitudes, e.g. the SLF is 40% below the global average in Vancouver of Canada, and 32% below in Rotterdam, in the Netherlands.

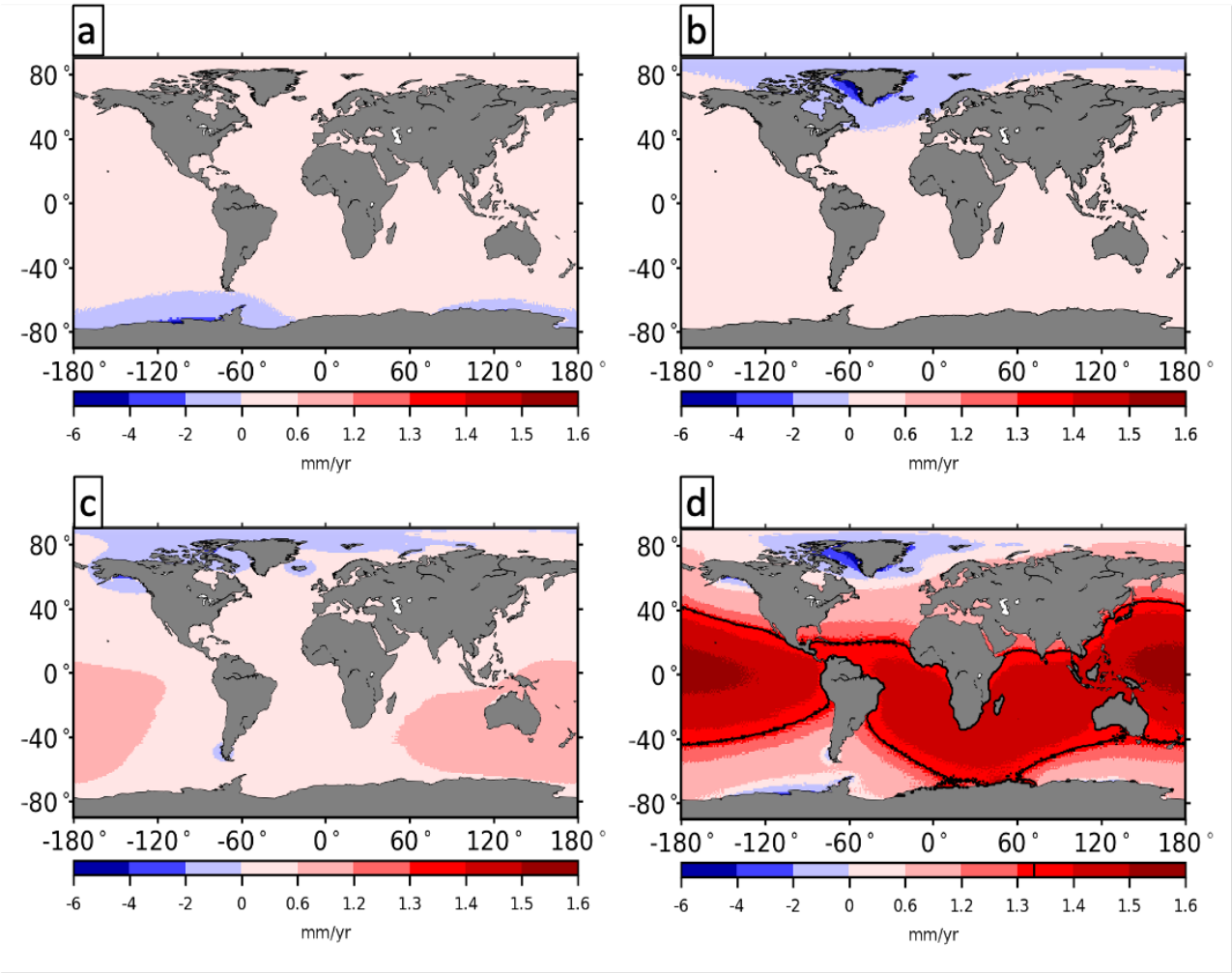

Figure 2.9: Trend of sea level fingerprint (SLF) for 1980-2019 from a) Antarctica, b) Greenland, and c) glaciers and ice caps (GIC); d) SLF 40-year trend contributed by total land-ice with a rate of global mean sea level rise of 1.33 m/yr (black contour line).

2.5 Discussion

We compare our results of annual mass balance (i.e., dM/dt) for six major GIC with independent estimates from the geodetic and glaciological techniques [*Zemp et al.*, 2019] over the common time period of 1980-2016, excluding the glaciers peripheral to Greenland and Antarctica which are already included in our MBM and GRACE estimates, and Patagonia North and South Ice Fields where the glacier domains differ from our study (Figure 2.12 and Table S5). The dM/dt of this study is defined as the trend each year derived from

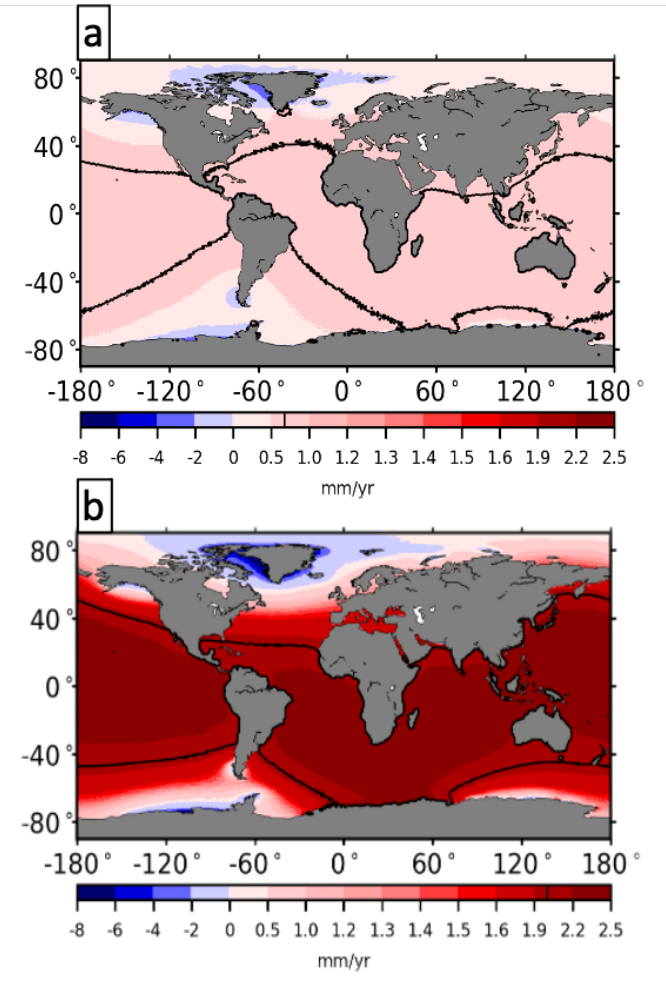

Figure 2.10: Comparing trend of total land-ice SLF over the first twenty years (1980-1999) and the last twenty years (2000-2019). The global mean sea level rise rate (black contour line) for these two time periods are 0.67 mm/yr v.s. 2.0 mm/yr.

of the 13-month smoothed cumulative monthly time series. The associated error is calculated using a Monte Carlo approach which propagates the cumulative monthly errors on the annual dM/dt through the 13-month smoothing process. We find an average mass loss of of the six GIC regions of 160 Gt/yr versus 169 Gt/yr from *Zemp et al.* [2019]. We find a reasonable agreement in Alaska and Canadian Arctic Archipelago. The largest discrepancies are recorded in High Mountains of Asia, Iceland, Russian Arctic, and Svalbard Island. For Iceland and Svalbard Island, the difference is due to an offset in SMB. Our estimates from multi-models have an error at the 4% level for Iceland and 25% for Svalbard Island (Table

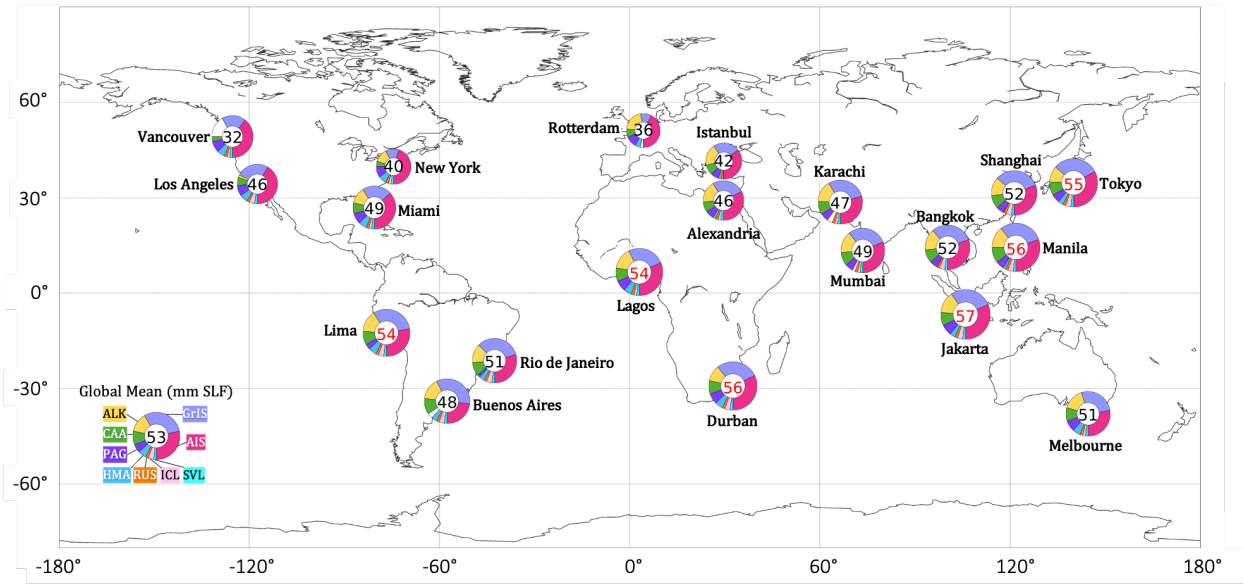

Figure 2.11: SLF change from 1980 to 2019 at selected coastal cities at high risk of sea level rise. The donut chart the lower left corner represents the global mean contributions with its size corresponding to cumulative sea level rise of 53 mm. Value at the center of each donut chart is total SLF change from land-ice, colored red if above the global mean of 53 mm and black otherwise. Wedge areas are the contributions from Greenland (GrIS), Antarctica (AIS) and the GIC regions (ALK = Alaska, CAA = Canadian Archipelago, PAG = Patagonia, HMA = High Mountain Asia, RUS = Russian Arctic, ICL = Iceland, SVL = Svalbard Island). White wedges are negative contributions (e.g. ALK to Vancouver, PAG to Buenos Aires, ICL to Rotterdam, HMA to Karachi, and HMA to Mumbai.)

2.3). In the Russian Arctic, we have an excellent agreement in SMB interannual variability between MERRA-2 and GRACE [*Ciracì et al.*, 2020], which is not reproduced by the geodetic and glaciological techniques. In High Mountains of Asia, we are in better agreement with GRACE in terms of interannual variability, but it is difficult to conclude on the most accurate representation of the mass loss. Over the common GRACE time period, our results agree, but we find differences in the estimates for the earlier period which is when *Zemp et al.* [2019] use old topographic maps with large uncertainties.

We compare the global mean sea level (GMSL) from our component approach with the GMSL from altimetry [*Cazenave et al.*, 2018b] for the time periods 1993-2015 and 2005-2015 and also with another study based on a statistical modeling [*Frederikse et al.*, 2020a] for the time period 1980-2018. The goal of the comparison is to determine if our revised ice mass budget

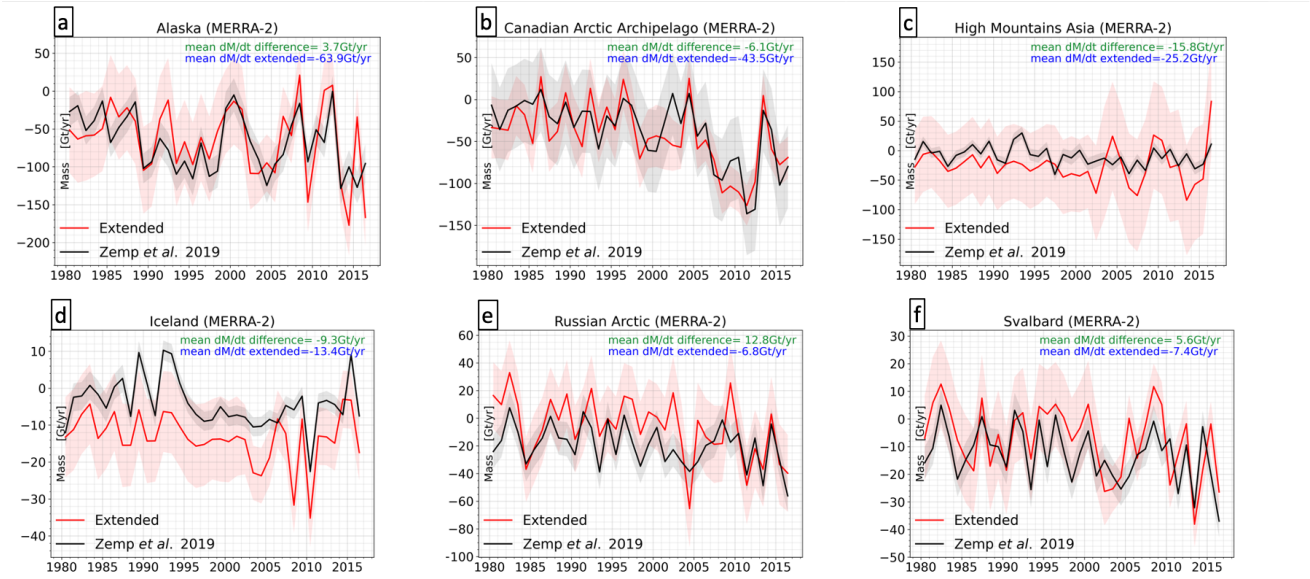

Figure 2.12: Comparison of annual time series of mass loss, dM/dt, for the GIC from *Zemp et al.* [2019] versus this study, excluding the Patagonia North and South Ice Fields. 'Mean dM/dt diff' is the mean dM/dt from this study minus *Zemp et al.* [2019] for the time period 2003-2016 (i.e., overlapping time period of both studies). 'Mean dM/dt ref' is the reference dM/dt of GRACE during the period 2003-2016. The dM/dt of this study is defined as the trend each year derived from of the 13-month smoothed cumulative monthly time series. The associated error is calculated using a Monte Carlo approach which propagates the cumulative monthly errors on the annual dM/dt through the 13-month smoothing process.

improves the sea level budget closure 2.5. Ocean altimetry documents a GMSL of 3.07±0.22 mm/yr for 1993-2015 versus a sum of thermal expansion and melting land ice of 2.7±0.27 mm/yr in [*Cazenave et al.*, 2018b], which leaves 0.37±0.35 mm/yr unaccounted for which they attribute to uncertainties in terrestrial water storage (TWS). In our revised estimates, the contribution from land ice and thermal expansion is slightly larger, at 2.94±0.30 mm/yr, and the residual is reduced by a factor 3 from 12% to 4%. The improvement is attributed to our estimated larger loss from Antarctica. In *Frederikse et al.* [2020a], it was found that most changes in TWS took place in the 1970s and ended around the 1980s, hence the long-term TWS component should be negligible for 1980-2019 and 1993-2015.

Over the period of 2005-2015, the agreement between observed GMSL and the sum of thermal expansion and melting of land-ice is also improved. The difference between our estimates and

	1980-2018		1993-2015		2005-2015	
	This paper	F20	This paper	C18	This paper	C18
1. GIC	0.54±0.04	0.59±0.09	0.61±0.04	0.65±0.09	0.69±0.16	0.74±0.06
2. Antarctica	0.38±0.09	0.23±0.07	0.53±0.17	0.25±0.06	0.72±0.39	0.42±0.06
3. Greenland	0.36±0.03	0.42±0.05	0.50±0.05	0.48±0.06	0.79±0.13	0.76±0.06
4. Land ice	1.27±0.10	1.24±0.20	1.64±0.18	1.38±0.12	2.21±0.44	1.92±0.10
5. Thermosteric	0.81±0.12*	0.81±0.12*	1.3±0.24+	1.3±0.24+	1.3±0.24+	1.3±0.24+
6. Land-ice + thermosteric	2.08±0.16	2.05±0.28	2.94±0.30	2.7±0.27	3.51±0.50	3.22±0.26
7. GMSL	2.72±0.27*	2.72±0.27*	3.07±0.22+	3.07±0.22+	3.5±0.12+	3.5±0.12+

Table 2.5: Contributions to sea level rise trend in mm/yr from the glaciers and ice caps (GIC), Antarctica, Greenland, and thermalsteric versus the observed global mean sea level (GSML) from this study, *Frederikse et al.* [2020a] (F20, denoted as *), and *Cazenave et al.* [2018b] (C18, denoted as +). The F20 numbers are for 1980-2018. The C20 numbers are from Table 12 and 13 in *Cazenave et al.* [2018b]. Errors are at the 68% confidence level.

the observed GMSL is only 0.01 mm/yr versus 0.28 mm/yr in *Cazenave et al.* [2018b], again due to a larger contribution from Antarctica. Over the longer time period 1980-2018, we have lower estimates of mass loss for Greenland and GIC, and higher for Antarctica, but the total loss agrees with the estimates from *Frederikse et al.* [2020a]. Both estimates however fall short of the observed GMSL prior to 1993, which is not based on ocean altimetry.

Over the longer time period 1980-2018, we have lower estimates of the loss for Greenland and GIC, but higher losses for Antarctica, which compensate each other to generally agree with *Frederikse et al.* [2020a]. For Greenland, our estimates are based on a complete reconstruction of SMB and discharge whereas *Frederikse et al.* [2020a] rely on the comparison of digital elevation models. Similarly, for the GIC, we rely on SMB models instead of elevation models. Both estimates fall however relatively short of the observed GMSL. The observed GMSL however has no ocean altimetry data prior to 1993.

Our calibration of the SMB models for the GIC regions with GRACE data is equivalent to an evaluation of the SMB models at a world wide scale. While the models tend to reproduce the seasonal to interannual variability in SMB well, the calibration offsets are generally large, e.g. 11 Gt/yr in Canadian Arctic Archipelago versus a mass loss of 44 Gt/yr 2.6. The

exercise therefore indicates that GRACE/GRACE-FO data remain essential to calibrate these climate models and reduce the uncertainties in cumulative mass loss. With a longer time series of GRACE/GRACE-FO data, the model evaluation could be improved and the uncertainties in reconstructed SMB could be reduced.

Table 2.6: Comparison of annual mass balance (i.e., dM/dt) values between *Zemp et al.* [2019] and the results of this study. The dM/dt of this study is defined as the trend each year derived from of the 13-month smoothed cumulative monthly time series. The associated error is calculated using a Monte Carlo approach which propagates the cumulative monthly errors on the annual dM/dt through the 13-month smoothing process. The difference is the value from our study minus the value in *Zemp et al.* [2019]. The dM/dt difference in percentage is calculated as the dM/dt difference divided by the reference dM/dt, where the reference dM/dt is the annual mass balance of this study reconstructed using MERRA-2 for all GIC regions. Patagonia North and South Ice Fields is not included in this comparison as the glacier domain differs a lot in the two studies.

	ALK	CAA	HMA	ICL	RUS	SVL
dM/dt difference [Gt/yr]	3.7	-6.1	-15.8	-9.3	12.8	5.6
Reference dM/dt [Gt/yr]	-63.9	-43.5	-25.2	-13.4	-6.8	-7.4
dM/dt difference (%)	6%	14%	63%	69%	188%	76%

For Greenland, the mass balance estimates from various methods are in excellent agreement [*Shepherd et al.*, 2020], so future improvements in mass balance estimates will likely be marginal. In Antarctica, residual differences exist in East Antarctica. The altimetry estimates suggests modest growth in the interior combined with thinning of a few basins at low elevations [*Smith et al.*, 2020]; the GRACE estimates indicate a small mass gain affected by uncertainties in GIA; and the MBM indicates a mass loss along the periphery. Our comparison with the sea level budget suggests that Antarctica probably contributed more to the GMSL than estimated previously, which is consistent with the higher losses from the MBM method. A state of mass loss for a number of East Antarctic glaciers is also corroborated by satellite altimetry observations of ice thinning (e.g. [*Smith et al.*, 2020]) and observations of mass loss at the sub-basin level from GRACE and MBM ([*Mohajerani et al.*, 2018] and [*Mohajerani et al.*, 2019]). Conversely, the state of mass balance of the plateau is indicated as positive from altimetry in 2003-2019 (e.g. [*Smith et al.*, 2020]), less positive

from GRACE/GRACE-FO in 2002-2019 [*Velicogna et al.*, 2020], and negligible in 2002-2019 from the SMB models [*Rignot et al.*, 2019]. Additional research and observations are needed to resolve these residual uncertainties in East Antarctica.

The longer record of SLFs reconstructed herein will be instrumental for detecting the land ice melt signal in the tidal gauge record [*Davis and Vinogradova*, 2017] since it triples the duration of the previous record and therefore makes the land ice melt signal larger than the background noise from the natural variability of the system. Detecting SLFs in the observing sea level signal would in turn provide additional confidence in the SLF methodology and the reconstructions of its components and its geographic sources.

2.6 Conclusions

We present a 40-year record of land-ice mass changes from the world's major GIC, Greenland, and Antarctica that combines GRACE/GRACE-FO data, MERRA-2/GEOS-5 data, multiple other regional and global climate model ouputs, and reconstructions of ice discharge from the marine-terminating glaciers in Greenland and Antarctica, that triples the observation period of SLF compared to the previous estimates based on GRACE/GRACE-FO alone, with improved confidence in the estimates during the common time period. Overall, the GIC contributed a larger mass loss than Greenland and Antarctica, but the difference between them is small. The contribution of ice sheets has been rapidly accelerating and now dominates the sea level signal, so that over the last four decades, the three components have contributed almost equally to total sea level change. At present, the dominant signal is from the ice sheets but the GIC signal remains significant and cannot be ignored. We expect the 40-year SLF record to be of importance for comparison with other land observations to better understand the components of sea level change, its geographic distribution, and help in turn improve projections of future sea level change.

Chapter 3

2005-2019 Sea Level Budget Evaluation

3.1 Abstract

Multiple processes are contributing to present sea level changes. The processes include thermal and haline (i.e., salinity related) expansion and contraction, land ice melting, land water storage changes, and atmospheric and dynamical ocean loading changes. The total sea level can be estimated in two methods: 1) direct measurement of sea surface height by altimetry and 2) the sum of individual sea level components. The evaluation of the balance of total sea level obtained from the two methods is referred to as sea level budget closure estimate. Closure of the sea level budget indicates that the total sea level change can be explained with the observed processes without missing components. In this study, we use multiple state-of-art observations, including satellite and in-situ measurements, to estimate contributions from individual sea level components to the total sea level over 2005-2019 and compare the sum of the individual components to total sea level at the global mean

and basin mean level. We find an excellent agreement within 7% between the sum and the total sea level at the global mean and Pacific ocean basin level, suggesting closure of sea level budget. However, in the Indian Ocean and Atlantic Ocean basins, the sum differs significantly from the total, suggesting unaccounted components or missing processes (e.g., potential deep ocean warming, anthropogenic impacts on groundwater). We also compared the relative contribution from different components to the total trend and find ice sheets melting and steric expansion being the leading contributors across different basins and at the global mean level.

3.2 Introduction

The sea level budget equation can be written as:

$$SL_{Total} = SL_{LandIce} + SL_{LandWater} + SL_{Steric} + SL_{AtmosPres} + SL_{OceanDyn} + SL_{Uncertainty} \quad (3.1)$$

Where SL_{Total}, $SL_{LandIce}$, $SL_{LandWater}$, SL_{Steric}, $SL_{AtmosPres}$, $SL_{OceanDyn}$, $SL_{Uncertainty}$, are total sea level, sea level caused by land ice mass changes, sea level caused by land water storage changes, sea level caused by ocean density changes (i.e., steric sea level), sea level caused by atmospheric pressure changes, sea level caused by dynamical ocean processes, and uncertainties. Here for the dynamical ocean processes, we will not consider the tidal impact on the sea level because tidal impacts are mostly happening within a month, but the scope of this study is at a temporal scale that is longer than monthly scales.

Evaluating the closure of sea level budget based on observations is important in multiple aspects. Sea level budget estimates can be used to calibrate and validate model physics, for example, the glacial isostatic adjustment (GIA) process, which is crucial for enhancing accuracy in gravimeter (GRACE/GRACE-FO) measured mass changes in Antarctic Ice Sheet.

Observations of past and ongoing contributions to total sea level from different sea level components provides constrain on predictions of future sea level rise. Moreover, the level of closure helps quantify possible under-studies processes, including potential deep ocean warming and anthropological influences on terrestrial water storage changes (e.g., groundwater extraction, reservoir impoundment). Sea level budget evaluation also facilitates estimation of energy budget imbalance [*Von Schuckmann et al.*, 2016b].

Previous evaluations on sea level budget have reached a closure on the global mean level in the satellite era (1993-2018) but with large uncertainties in land-water contributions [*Cazenave et al.*, 2018b]. Part of the uncertainties arises from a lack of reliable measurement and simulations of anthropogenic impacts on land water, for instance, groundwater withdrawal, impoundment, land cover and land-use change, deforestation and afforestation, wetland degradation, lake storage changes, as well as human impacts on water cycle variability [*Chao et al.*, 2008; *Wada et al.*, 2012; *Döll et al.*, 2016; *Zhao et al.*, 2021]. Most land water storage measurements and simulations can only observe individual hydrology components (e.g., runoff, precipitation), or they mainly obtain changes in the surface layer of the terrestrial water column. We use total water storage measurement from GRACE and GRACE-FO satellites which provide a more comprehensive picture of the net changes in the whole vertical soil column. Here we improve the spatial variability obtained from GRACE/GRACE-FO using ad-hoc scaling factors. We continue using the reconstructed land ice mass changes from the mass budget method (MBM) for ice sheets and GRACE/GRACE-FO for glaciers and ice caps for land ice measurements. Land ice melting is one of the most significant contributors to total sea level rise. Our land-mass changes record is the state-of-art measurement-based datasets which incorporate the latest version of MBM data [*Mouginot et al.*, 2019] and the most accurate estimate of glaciers and ice caps using GRACE spherical harmonics mascon approach [*Ciracì et al.*, 2020]. Another major sea level component is the steric sea level, which reflects ocean volume's thermal and haline expansion and contraction in response to temperature and salinity changes. The ARGO floats are by far the most advanced observa-

tions on temperature and salinity as well as other oceanic conditions since 2000 [*Roemmich and Gilson*, 2009]. We calculate steric sea level changes using temperature and salinity data provided from the SCRIPPS Institution of Oceanography which has the most reliable product among three other processing centers, which filtered out an instrumental drift error since 2016 [*Barnoud et al.*, 2021] and thus helped minimize artificial signal in the budget estimate. In addition, we also account for sea level fingerprint (SLF) changes induced by loading variations in the atmospheric and oceanic non-tidal dynamical processes, which has the smallest contribution to total sea level but helps complete the sea level budget comparison with all available observations. We compare the sum of the individual sea level components to the total sea level represented by GIA-corrected sea surface height, obtained from altimetry measurements.

3.3 Data and Methodology

3.3.1 Land Mass Sea Level Fingerprints

Land-mass variations caused changes in the sea level fingerprints. Here land-mass refers to the sum of land ice and terrestrial water storage. We continue to use the same land-ice mass changes fields as in Chapter 2. Monthly land ice mass changes are used as input fields for sea level fingerprints as in this chapter, we concern not only about the long-term changes (i.e., trend, cumulative changes, and inter-annual variability) but also seasonal to annual changes. As we aim to examine the balance of the sea level budget using mainly observation-based data sets, we do not use bridge the gap year (i.e., July 2017 - May 2018) between the GRACE and GRACE-FO mission as in Chapter 2. However, this less than one year gap will not significantly impact the temporal analysis, given we have high-quality observations of 15 years. We also use the same monthly errors of land ice mass changes

defined in Chapter 2 and then propagate the error on mass to error on SLF using a Monte Carlo approach. We calculate trend SLF trend caused by total land ice mass variations from Greenland and Antarctica ice sheets and seven major glaciers and ice caps (Figure 3.1). We estimate the trend from monthly ice sheets mass anomalies by simultaneously fitting a trend, acceleration, constant, annual, and semiannual signals to the gridded time series following the regression approach in *Velicogna* [2009]. The global mean equivalent SLF trend of total land ice is 2.14 mm/yr.

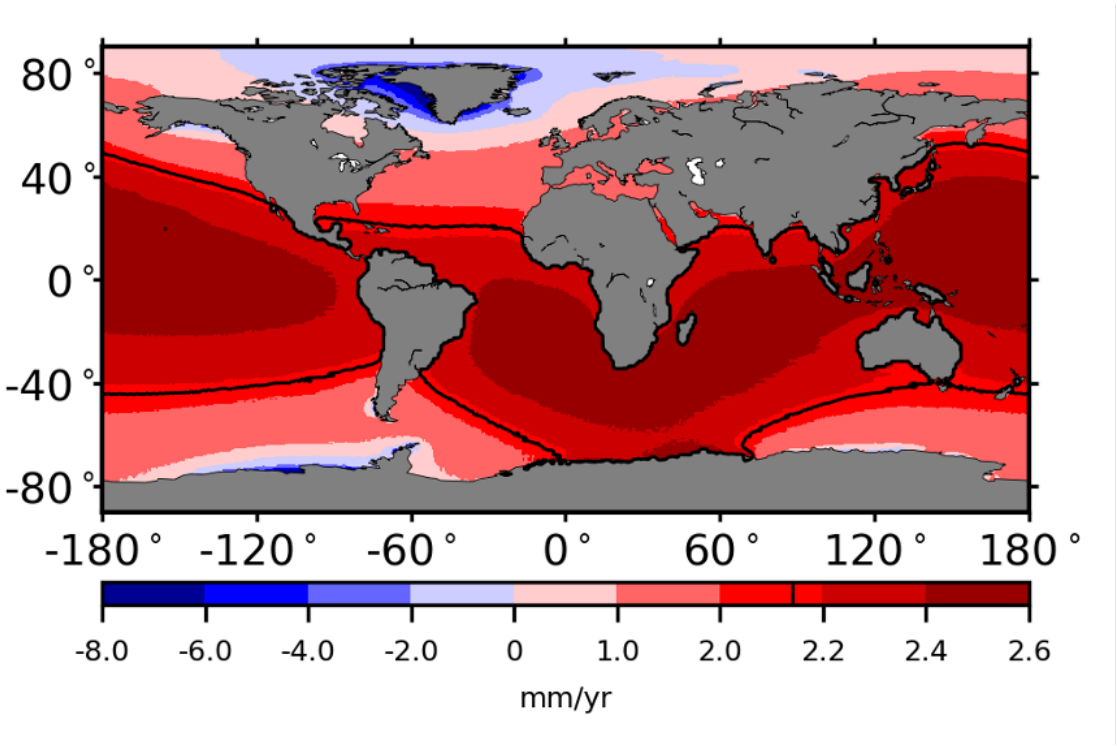

Figure 3.1: SLF trend over 2005-2019 caused by total land ice mass changes from Greenland and Antarctica ice sheets and seven major glaciers and ice caps. Black contour line indicates a global averaged trend of 2.14 mm/yr.

For terrestrial water storage (hereafter refers to "TWS"), we use ad hoc scaling factors to retrieve the signal from GRACE and GRACE-FO data following *Hsu and Velicogna* [2017]. Figure 3.2 compares TWS trend fields over April 2002 to December 2016 obtained directly from Community Land Model version 5.0 hydrological model (CLM5, *Lawrence et al.* [2019]) TWS (Figure 3.2a.) and GRACE-alike-processed (i.e., converting from spatial fields to stokes

coefficients, truncating, de-striping, smoothing with a Gaussian function, and converting back the spatial fields) CLM5 TWS (Figure 3.2b.). 2002-2016 is the overlapping period of the CLM5 model and GRACE/GRACE-FO data. CLM5 is used as a land component in multiple global and regional models, including being part of the Community Earth System Model (CESM) [*Lawrence et al.*, 2019]. We use the variable "total water storage" from the CLM5 model, which updates the previous versions of the CLM model's parameterizations and adds new hydrology processes, such as a revised groundwater scheme [*Lawrence et al.*, 2019]. After the GRACE-processing, TWS spatial pattern smooths out, and the signal amplitude gets attenuated. ([*Rodell et al.*, 2009; *Landerer and Swenson*, 2012; *Velicogna and Wahr*, 2013].) The trend field is calculated using a multi-linear regression. We simultaneously fit a trend, an annual, a semiannual, a constant, and the residual signals on each grid point.

Scaling factors are designed to restore the magnitude of the processed signal. To find out how much signal has been reduced, we apply the same GRACE and GRACE-FO processing procedures on a synthetic TWS field obtained from CLM5. We then compared the resulting TWS field with the original TWS field to calculate the scaling factors. To better account for hydrological processes with different spatial patterns and temporal variability, we apply two scaling factors. We use one scaling factor to restore the trend and inter-annual variability (Figure 3.3b.), and another scaling factor to recover the short-term changes that vary on the annual to sub-annual scales (Figure 3.3a.).

Scaling factors are sensitive to localized mass changes, for example, groundwater extraction signals from a water basin or glaciers melting signals near a coastline. The CLM TWS fields contain not only the liquid water on land but also land ice components. We choose to mask out land ice from the CLM model domain as hydrological model outputs do not provide realistic land ice mass changes. Our mask covers the whole Greenland and Antarctic ice sheets domains as in the MBM data. The mask contains the complete glaciers and ice caps domain based on the Randolph Glacier Inventory [*Pfeffer et al.*, 2014], which has an

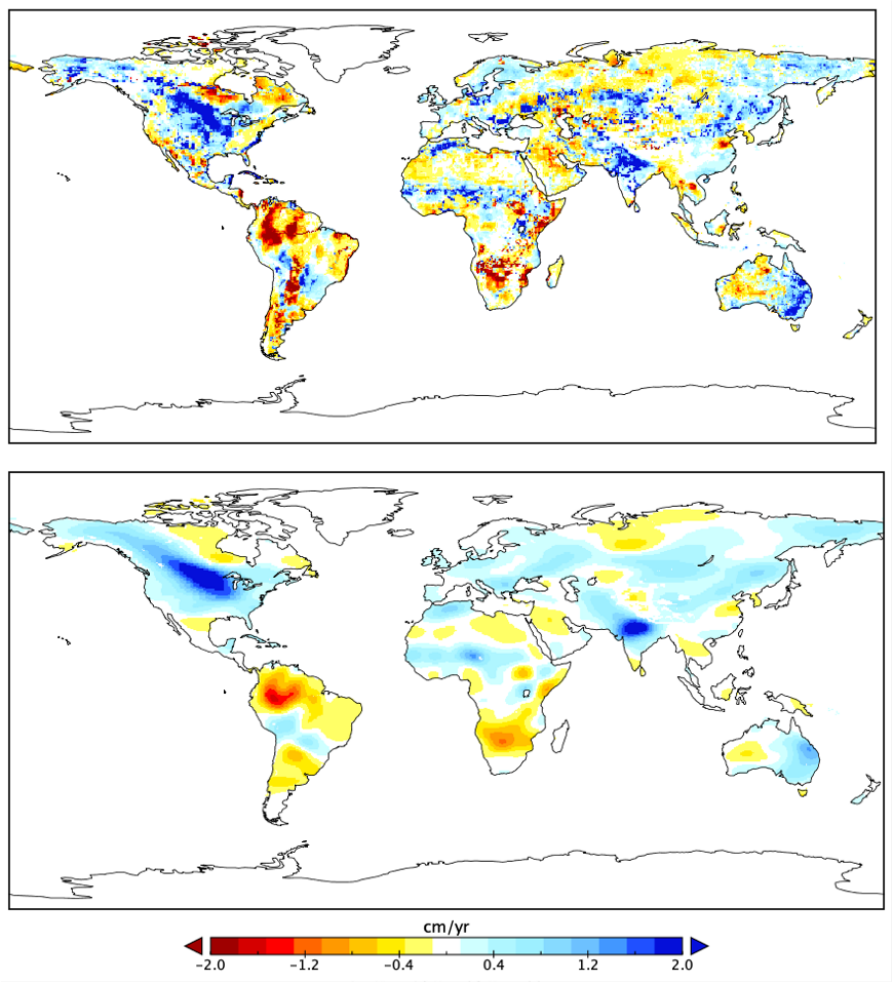

Figure 3.2: Trend of TWS from CLM5 from April 2002 to December 2016. a) The original TWS field. b) TWS fields with the GRACE processing (i.e., truncate, destripe, and smooth) being applied. TWS spatial pattern smooths out, and the signal amplitude gets attenuated after the GRACE processing.

entire ice-covered domain. Thus the domain area is larger than the seven major GIC regions studies in Chapter 2. Moreover, we account for the misrepresentation of model simulations on permafrost by identifying a threshold to remove abnormally high values in the model TWS outputs.

The scaling factor is calculated in the following manner. First, the CLM TWS field was decomposed to a long-term (trend, inter-annual) and a short-term (annual to sub-annual) field through a 13-month smoothing approach [*Velicogna and Wahr*, 2013]. The GRACE processing steps are employed on the two fields, respectively. On each grid point, a scaling

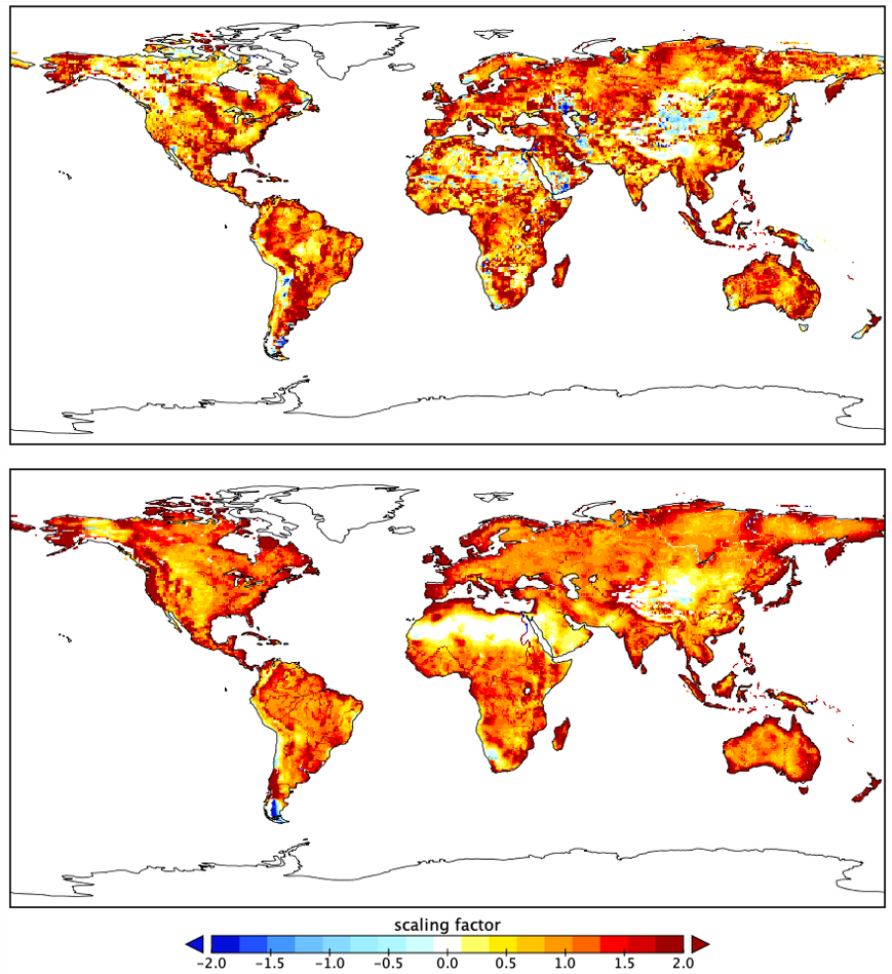

Figure 3.3: Scaling factors calculated using synthetic fields of TWS from CLM5 model. a) Scaling factors for restoring the short-term signals that varies on the annual to sub-annual scales. b) Scaling factors for restoring the long-term signals of trend and inter-annual variability.

factor of either the long-term field or the short-term field is defined as the sum of the product of the processed synthetic field with the unprocessed synthetic field divided by the sum of squares of the processed synthetic field. We select Riyadh (24.75N,46.75E), the capital city of Saudi Arabia, to provide a localized view of modeled TWS being decomposed into a smoothed signal and the residuals (Figure 3.4a.), and a comparison between the original, GRACE-processed, and the restored TWS from CLM5 (Figure 3.4b.). GRACE-processing's impact on the long-term and short-term signals varies by geographical location. For example, the processing has a strong attenuation effect on the trend and inter-annual signals than on

the annual and sub-annual signals at Riyadh, with the corresponding scaling factors of 3.6 and 0.7.

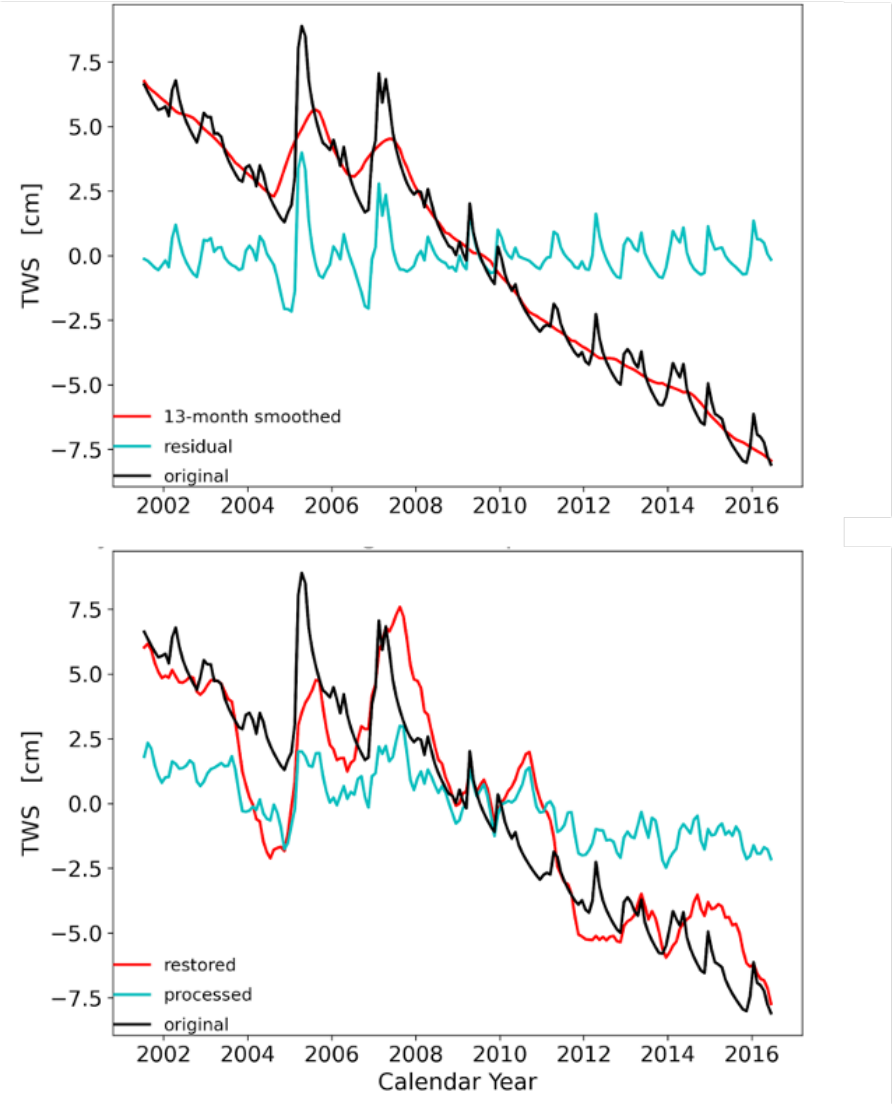

Figure 3.4: CLM5 TWS being decomposed into a smoothed signal and the residuals (a), and a comparison between the original, GRACE-processed, and the restored TWS from CLM5 (b) at Riyadh. GRACE-processing has a strong attenuation effect on the trend and inter-annual signals than on the annual and sub-annual signals at Riyadh, with the corresponding scaling factors of 3.6 and 0.7.

Then we decompose the GRACE and GRACE-FO field using a simple linear fit, where we obtain a trend field and a residual field. The residual field is defined as the remaining signal from GRACE and GRACE-FO TWS after removing the trend field. To recover the TWS

signal, we multiplied the long-term scaling factor with the GRACE and GRACE-FO trend field and multiplied the short-term scaling factor with the GRACE and GRACE-FO residual field. The scaling factors are applied to each grid point of the GRACE/GRACE-FO TWS spatial field. Eventually, we add up the recovered trend field and the residual field to fully restore the GRACE and GRACE-FO TWS signal. Figure 3.5 a and b compares GRACE TWS global trend patterns estimated over 2002-2016 before and after scaling factors being applied to the TWS field. The restored GRACE TWS trend map has finer spatial details and higher signal amplitude as expected. Again, we choose Riyadh to provide a localized view of how the trend and residual scaling factors have worked on restoring GRACE signals (Figure 3.6). The scaling factors notably restored the GRACE TWS time series trend as the long-term signal scaling factor (3.6) is far greater than one. In contrast, the residual signals (annual and sub-annual) do not have notable changes as a close to one (0.7) scaling factor is applied to the short-term part of the GRACE signal. We applied the scaling factors from 2002-2016 to the GRACE/GRACE-FO TWS field over 2002-2019. We use the restored GRACE/GRACE-FO TWS field as an input mass changes field to calculate the associated SLF. We calculate the SLF trend caused by TWS mass changes over 2002-2019 (Figure 3.7). We estimate the trend from monthly terrestrial water storage mass anomalies by simultaneously fitting a trend, acceleration, constant, annual, and semiannual signals to the gridded time series following the regression approach in *Velicogna* [2009]. The global mean equivalent SLF trend of TWS is 0.45 mm/yr. We find a faster increase in sea level in the southern hemisphere.

The uncertainties of GRACE/GRACE-FO TWS result from the uncertainty in the scaling factors and GRACE/GRACE-FO measurement errors. The GRACE/GRACE-FO measurement errors are calculated as the root mean square (RMS) between the restored GRACE/GRACE-FO TWS and the smoothed restored GRACE/GRACE-FO TWS. The smoothed GRACE/GRACE-FO TWS is the long-term trend and inter-annual variability signals decomposed from the total GRACE/GRACE-FO TWS. The uncertainty in the scaling factor is defined as the

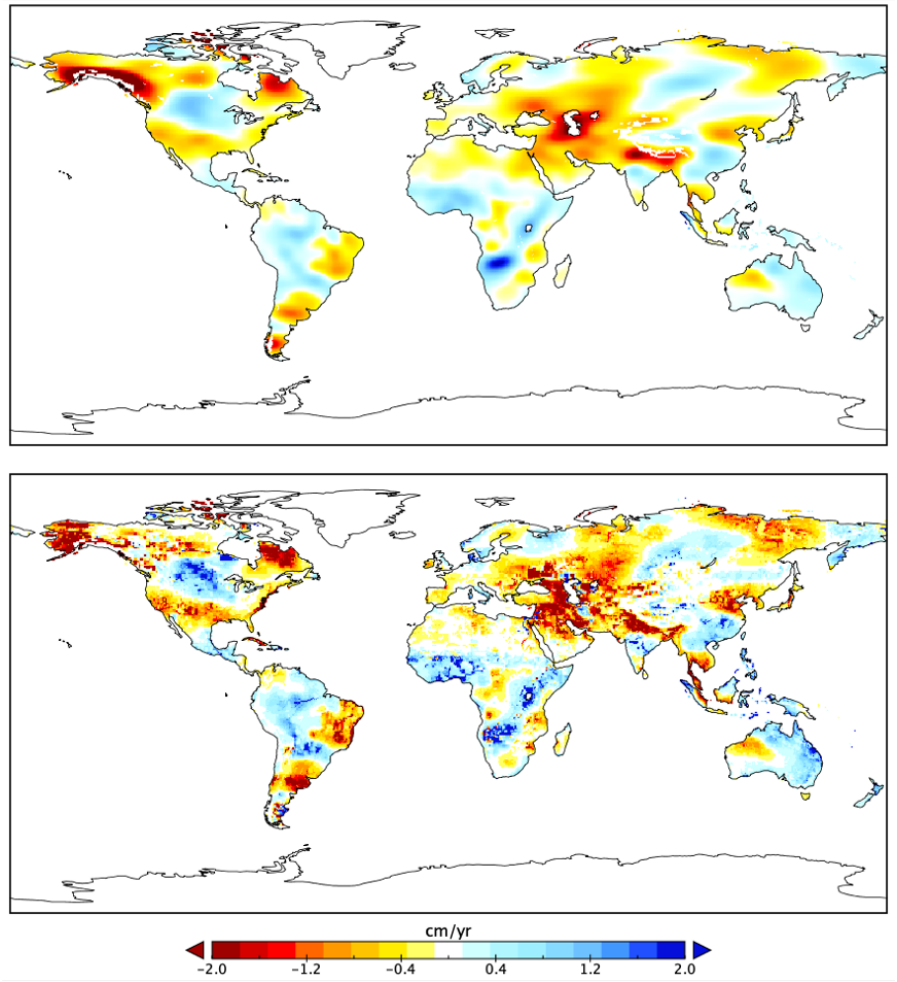

Figure 3.5: GRACE TWS global trend patterns estimated over 2002-2016 before (a) and after (b) scaling factors being applied to the TWS field.

GRACE/GRACE-FO TWS RMS scaled by the scaling factors and then follows the error propagation law [*Hsu and Velicogna*, 2017; *Landerer and Swenson*, 2012; *Wahr et al.*, 2006; *Swenson et al.*, 2008; *Velicogna and Wahr*, 2013]. The error of scaling factor is calculated as:

$$error = \frac{RMS(syn_{ori} - factor_{long} \times syn_{procL} - factor_{short} \times syn_{procS})}{syn_{ori}} \times RMS(GRACE_{restored}) \tag{3.2}$$

Where syn_{ori}, syn_{procL}, syn_{procS} are the original synthetic field (i.e., TWS from CLM5),

the long-term signal of the synthetic field after the GRACE processing being applied to the original CLM5 TWS, the short-term signal of the synthetic field after the GRACE processing. $factor_{long}$ and $factor_{short}$ are long-term and short-term scaling factors. $GRACE_{restored}$ is the scaled GRACE/GRACE-FO TWS field. We calculate an error on each grid point within the TWS domain. Figure 3.8 and Figure 3.9 show spatial fields of the long-term (trend) and residual (i.e., inter-annual, annual, and sub-annual signals) errors in TWS due to uncertainties in the corresponding scaling factors.

We then propagate the monthly TWS error to SLF error using a Monte Carlo approach following *Hsu and Velicogna* [2017]. We generate 1,000 values following a Gaussian pseudo-random distribution with a standard deviation equal to the TWS monthly error on each grid cell. After that, on each grid cell, we calculate 1,000 SLF. Finally, the SLF monthly error (1 σ) at each grid cell is calculated as the standard deviation of 1,000 SLF values. We calculate the SLF trend error and residual error following the same procedure.

3.3.2 Atmospheric and Oceanic Non-tidal Loading Sea Level Fingerprints

Atmospheric and oceanic non-tidal loadings are high-frequency (shorter than a few months), irregular pressure changes in the atmosphere, and mass redistribution of ocean water, which can change sea level [*Paul Boy and Lyard*, 2008; *Boy et al.*, 2009]. In comparison, tidal loading effects refer to the periodic displacement of sea level due to external forces from the Sun and Moon, and pole tide in response to the Earth rotation [**?**]. We use GRACE/GRACE-FO monthly Atmospheric and Ocean Dealiasing Level 1B (AOD1B) gridded products from the Jet Propulsion Laboratory (JPL), which captures the time-variable gravity potential signal caused by atmospheric and oceanic non-tidal loading mass changes. JPL AOD1B product contains four types of AOL data (i.e., GAA, GAB, GAC, and GAD) [*Chen et al.*, 2019].

GAA and GAB refer to atmospheric non-tidal loading field and oceanic non-tidal loading field, respectively. GAC represents total non-tidal loading caused by the atmospheric and oceanic mass variations (i.e., GAC = GAA + GAB). GAD is similar to GAC, but with signals on land grid points masked out. We choose GAC to account for atmospheric and oceanic non-tidal loading signals over both land and ocean. The Integrated Forecast System of the European Centre for Medium-Range Weather Forecasts (ECMWF) provides the atmospheric loading fields calculated using their meteorological analysis fields at 6 hours temporal resolution [*Dobslaw et al.*, 2017; *Fagiolini et al.*, 2015]. Ocean Model for Circulation and Tides (OMCT) provides the oceanic loading fields with mass conservation in the global ocean [*Thomas*, 2002]. All four types of AOL data have been processed like GRACE/GRACE-FO in the spherical harmonics domain. The data has been truncated to different degrees and orders, smoothed with Gaussian smoothing function of different radius, and then combined to generate the gridded product. We choose GAC with truncation to degree and order up to 60 degrees and smoothed with a 300 km radium so that the Atmospheric Oceanic Non-tidal Loading signal is comparable to other GRACE-derived loading fields (i.e., ice sheets, glaciers and ice caps, and terrestrial water storage over the GRACE/GRACE-FO period).

We use the GRACE/GRACE-FO atmospheric and oceanic non-tidal loading fields as input fields to generate the corresponding SLF. Then we estimate the trend of the obtained SLF from April 2002 to November 2019 (Figure 3.10). We estimate the trend from monthly steric sea level by simultaneously fitting a trend, acceleration, constant, annual, and semiannual signals to the gridded time series following the regression approach in *Velicogna* [2009]. The global mean SLF trend due to the atmospheric and oceanic non-tidal loading is -0.01 mm/yr.

3.3.3 Total Sea Level Fingerprints

We combine mass loading trends from Greenland and Antarctic ice sheets, glaciers and ice caps (GIC), terrestrial water storage (TWS), and atmospheric and non-tidal ocean loading (AOL) to calculate the total SLF trend. The equation of total SLF can be written as:

$$SLF_{Total} = SLF_{LandIce} + SLF_{LandWater} + SL_{AOL} \tag{3.3}$$

Where SL_{AOL} is SLF caused by non-tidal ocean loading, which includes impacts on sea level from atmospheric pressure changes and ocean dynamical processes (e.g., currents, waves). We calculate the total SLF trend caused by all land-mass variations (Figure 3.11) over 2002-2019. We estimate the trend of SLF by simultaneously fitting a trend, acceleration, constant, annual, and semiannual signals to the gridded time series following the regression approach in *Velicogna* [2009]. The global averaged sea level trend is 2.54 mm/yr. Regions within 40 degrees North and South generally witness an above-average sea level rise rate. Western to middle Pacific ocean and the west coasts of Southern Africa experienced the fastest sea level rise.

3.3.4 Steric Sea Level

Ocean density variations cause steric sea level changes. Changes in ocean temperature and salinity lead to ocean density changes, including expansion and contraction of the ocean volume, corresponding to a sea level increase and a decrease, respectively. Sea level changes associated with temperature changes are referred to as the thermosteric sea level changes. For instance, warmer ocean expanses and thus thermosteric sea level rises. Sea level changes associated with salinity changes are referred to as halosteric sea level changes. For example, with land ice and sea ice melting into the oceans, freshwater dilutes seawater, leading to a

decreased density and increased ocean volume. As a result, the halosteric sea level increases.

We use Argo floats observations [*Roemmich and Gilson*, 2009] of ocean temperature, salinity, and pressure to calculate the steric sea level. Four agencies process the ARGO float observations: SCRIPPS Institution of Oceanography, National Oceanic and Atmospheric Administration (NOAA), Met Office Hadley Center, and Japan Agency for Marine-Earth Science and Technology. We choose the temperature, salinity, and pressure data processed by SCRIPPS as the salinity product from the other three agencies are known to have a positive bias due to instrumental error since 2016, which would lead to an underestimation of the steric sea level (i.e., increased salinity causes increased density and decreased ocean volume and thus decreased halosteric sea level) [*Barnoud et al.*, 2021]. Argo team provides oceanic property data sets since 2000 on one-by-one degree latitude-longitude grids. Prior to 2005, Argo data had few measurements in the Southern Ocean [*Roemmich and Gilson*, 2009] [*Leuliette*, 2015]. As a result, we choose to use the data since 2005 when there is sufficient near-global coverage from 66 N to 60 S. The ARGO data reaches a depth of 2000 meters with a vertical resolution varying with depth. When it is closer to the sea surface, the vertical resolution is about 10 dbar. When it is closer to 2000 m, the vertical resolution becomes 100 dbar.

To derive the steric sea level changes, we first calculate the density profiles based on the Thermodynamic Equation of Seawater - 2010 (TEOS-10) [*McDougall and Barker*, 2011]. TEOS-10 includes equations on all thermodynamic properties of seawater. The equations are based on a Gibbs function formulation that allows different thermodynamic properties to be derived in a thermodynamically consistent fashion. The equations need to be used with caution to carefully differentiate what types of salinity and temperature are being used (e.g., practical salinity or absolute salinity; in-situ temperature, conservative temperature, or potential temperature) and which units are appropriate for a specific equation. This is especially important given the fact that ARGO data variables have been updated through

the years, and a misinterpretation of the variable or the seawater equation can lead to bias in the resulting sea level as we integrate the density profile.

For example, absolute salinity is adopted as the standard variable needed for calculations of density and other thermodynamic properties, whereas the practical salinity used to be the standard before 2009 [*McDougall and Barker*, 2011]. In addition, the two quantities are not simply proportional to each other. The latest Argo data provides practical salinity and in-situ temperature. Therefore we first convert the practical salinity (unites) to the absolute salinity (in g/kg), and convert the in-situ temperature (in degree C) to conservative temperature (also in degree C) as required for the in-situ density equation. Then we use the hydrostatic balance, which defines a balance between the vertical pressure gradient force (PGF) per unit mass and the acceleration due to gravity (G) and the relation between the steric height (H) and the dynamic height to derive the steric sea level changes as following in the equations, where dp is the pressure difference (in pascal) between every two vertical layers:

$$-\frac{dp}{dz} - \rho \times g = 0 \tag{3.4}$$

$$-\frac{dp}{\rho} = g \times dz \tag{3.5}$$

$$H = \int dz = -\frac{1}{g}\int_z \frac{dp}{\rho} \tag{3.6}$$

We calculate the trend of the steric sea level based on ARGO monthly fields from January

2005 to November 2019 (Figure 3.12). The last month of 2019 was excluded in the trend estimation due to abnormally high sea level values compared to the rest of the months. We estimate the trend from monthly steric sea level by simultaneously fitting a trend, acceleration, constant, annual, and semiannual signals to the gridded time series following the regression approach in *Velicogna* [2009].

We adopt an uncertainty of the global averaged, and basin averaged steric sea level of 3 mm per month from *Leuliette and Miller* [2009]. We propagate the monthly uncertainty to annual uncertainty, trend uncertainty, and cumulative change uncertainty using a Monte Carlo method following *Hsu and Velicogna* [2017]. We generate 10,000 values following a Gaussian pseudo-random distribution with a standard deviation equal to the monthly uncertainty on each grid cell. Then we calculate the annual errors, trend errors, and cumulative change errors at 68% confidence interval as the 1σ errors of the respective time series error distribution.

3.3.5 Total Sea Level

We use sea surface height for the total sea level record, which represents sea level variations about the earth's geoid. We obtain the sea surface height data from Copernicus Marine Environment Monitoring Service (CMEMS) catalog [*Von Schuckmann et al.*, 2016a; *Le Traon et al.*, 2017]. CMEMS is a major platform hosting data sets on the global and regional oceans obtained from satellite remote sensing observations, in-situ measurements, and model simulation outputs. We resample the original sea surface height from a fine solution of 1/12 by 1/12 degrees to 1 by 1 degree, which is of the same resolution of SLF results. The resample procedure is performed as a simple spatial average of every 12 grids along the latitude and longitude, excluding missing values on the original finer resolution field. To make the sea surface height data comparable to GRACE/GRACE-FO data, we apply the

standard GRACE/GRACE-FO processing procedures to the sea surface height data (i.e., converting from spatial fields to stokes coefficients, truncating, de-striping, smoothing with a Gaussian function, and converting back the spatial fields). The elevation of the ocean floor changes in response to Glacial Isostatic Adjustment (GIA) affects the sea level. Therefore, we correct a GIA trend for the sea surface data using the same GIA model outputs as in the glaciers and ice caps data processing. Earth's polar motion (i.e., variations in the earth's rotation axis) lead to pole tides. Pole tides are displacements of the earth's crust and oceans that influence the measured sea surface height. We, therefore, correct the pole tides effects from the total sea surface height by removing the pole tide trend calculated following *Desai et al.* [2015]. After the GIA and pole tide correction, we calculate the trend of the corrected sea surface height over 2002-2019 (Figure 3.13). We also correct the steric signal from the total sea level to obtain sea level changes caused by mass variations. We calculate the trend of steric corrected sea surface height (Figure 3.14). We estimate the trend from the corrected monthly sea surface height by simultaneously fitting a trend, acceleration, constant, annual, and semiannual signals to the gridded time series following the regression approach in *Velicogna* [2009]. The obtained trend field of steric corrected sea surface height spans from 79.5 °N to 64.5 °S as this is the available measurement coverage of ARGO data and the associated steric sea level field.

We adopt an uncertainty of the global averaged, and basin averaged sea surface height of 4 mm per month from *Leuliette and Miller* [2009]. We propagate the monthly uncertainty to annual uncertainty and cumulative change uncertainty using a Monte Carlo method following *Hsu and Velicogna* [2017]. We generate 10,000 values following a Gaussian pseudo-random distribution with a standard deviation equal to the monthly uncertainty on each grid cell. Then we calculate the annual errors and cumulative change errors at 68% confidence interval as the 1σ errors of the respective time series error distribution. For trend errors, we adopt the value of 0.6 mm/yr from *Hsu and Velicogna* [2017], and *Ablain et al.* [2009], which is a more conservative estimate than the results propagated from the monthly errors using the

Monte Carlo Approach.

3.4 Results

3.4.1 Sum of Sea Level Components

We sum up individual sea level fingerprint contributions with steric sea level and calculate the trend of the summed sea level field during the overlapping period of individual contributors (2005-2019). The spatial domain of the summed field is the overlapping area of the individual components, which is from 79.5 °N to 64.5 °S. The tropical middle to eastern Pacific and the east coast of North America, and the east coast of Asia near Japan (40 N) has the largest trend over the 15 years, whereas the southern to southern-east coast of Greenland and an ocean area near the Philippines witnessed the strongest sea level decrease (Figure 3.15). Some of the strongest trends are along the western boundary currents, for instance, Kuroshio and Gulf Stream. But the Eastern boundary currents along the east coast of the Pacific ocean also witness a strong trend signal, which differs from the strong signal along the western boundary of the Pacific on the trend map of sea surface height 3.13.

3.4.2 Sea Level Budget

We evaluate the closure of sea level budget at the global and regional scale by comparing the sum of individual sea level components during their overlapping time to the total sea level measured by sea surface height. To do so, we sum up SLF by ice sheets, glaciers and ice caps, terrestrial water storage, as well as atmospheric and oceanic non-tidal loading, with steric sea level from January 2005 to August 2019. We compare the sum to sea surface height within their overlapping spatial coverage from 80N to 65S. We compare time series

of sea level budget at the global mean scale and at three major ocean basins, including the Atlantic Ocean basin, the Pacific ocean basin, and the Indian Ocean basin. We define the ocean basin domain using a basin mask from NOAA NODC WOA13: World Ocean Atlas 2013 [*Locarnini et al.*, 2018]. The ocean basin mask is an objectively analyzed gridded product with full global coverage and depth from the surface down to 5500 meters. We use basin domains defined at the surface (0 meters).

At the global mean level 3.1, the trend of the sum of individual sea level components and sea surface height agree within 6% (i.e., 4.1 mm/yr from the sum v.s. 4.4 mm/yr from sea surface height) (Figure 3.16). To compare the trends, we set the month's sea level as zero for all sea level components. Ice sheets mass loss dominate the trend over the 15 years, contributing 1.6 mm/yr or 37% to the total (i.e., hereafter total sea level refers to sea surface height). Steric sea level changes are the second-largest trend contributor, with a rise of 1.3 mm/yr or 29% to the total. Glaciers and ice caps mass loss, terrestrial water storage decrease, and increased dynamical loading from atmospheric and oceanic non-tidal fields contribute 17% (0.7 mm/yr), 13% (0.6 mm/yr), and -2% (-0.1mm/yr) to the total trend, respectively. Then we compare the interannual variability of the sea level components by removing the trend, seasonal signal, sub-seasonal signal, and the mean value over 2005-2019 from each individual sea level component. We also smoothed the monthly time series to enhance visuals before regression. At global, residuals of terrestrial water storage contribute most of the inter-annual variability in the total sea level (Figure 3.17). Steric sea level also has a significant contribution to the inter-annual variability of sea surface height. In contrast, land ice and atmospheric and oceanic non-tidal loading have a marginal impact on the overall inter-annual variability. We find a root mean squared error (RMSE) of 3.7 between the sum of sea level components with sea surface height. To calculate the root mean squared error, we first smooth the monthly time series using a 13-month smoothing technique following *Velicogna and Wahr* [2013]. The obtained root mean squared error it reflects differences at a temporal resolution longer than sub-seasonal scales.

	Global mean	Pacific ocean	Atlantic ocean	Indian ocean
1. Steric	1.3	1.3	1.2	1.4
2. Ice sheets	1.6	1.7	1.4	1.7
2. Glaciers and Ice caps	0.7	0.7	0.7	0.8
3. Land water	0.6	0.6	0.5	0.6
4. Atmos. & non-tidal Ocean	-0.1	-0.1	-0.1	-0.2
5. Sum (1. + 2. + 3. + 4.)	4.1	4.2	3.7	4.3
6. Total sea level	4.4	4.5	5.2	3.1
7. Total - Sum	0.3	0.3	1.5	-1.2

Table 3.1: Contributions to sea level trend in mm/yr over 2005 to 2019.

At the ocean basin averaged scale, we estimate the sea level budget by comparing the trend, inter-annual variability, and root mean squared errors of smoothed monthly time series from the spatially averaged result of the Pacific Ocean, the Atlantic Ocean, and the Indian Ocean.

In the Pacific Ocean 3.1, the trend of the sum of individual sea level components and sea surface height has a high agreement within 7% (i.e., 4.2 mm/yr from the sum v.s. 4.5 mm/yr from sea surface height) (Figure 3.18). Ice sheets mass loss dominate the trend over the 15 years, contributing 1.7 mm/yr or 38% to the total sea level. Steric sea level changes are the second-largest trend contributor, with a rise of 1.3 mm/yr or 28% to the total. Glaciers and ice caps mass loss, terrestrial water storage decrease, and increased dynamical loading from atmospheric and oceanic non-tidal fields contribute 16% (0.7 mm/yr), 12% (0.6 mm/yr), and -1% (-0.1mm/yr) to the total trend, respectively. In terms of inter-annual variability, steric sea level and terrestrial water storage are the top two contributors (Figure 3.19). Contributions from land ice and atmospheric and oceanic non-tidal loading remain small. We find a root mean squared error (RMSE) of 6.6 between the sum of sea level components with sea surface height, indicating a relatively good match or a fair closure of the sea level budget in the Pacific ocean given both the RMS difference and trend difference are small.

In the Atlantic Ocean 3.1, the trend of the sum of individual sea level components and sea

surface height agree within 30% (i.e., 3.7 mm/yr from the sum v.s. 5.2 mm/yr from sea surface height) (Figure 3.20). Ice sheets mass loss is leading the trend over the 15 years but with a lower contribution of 1.4 mm/yr or 28% to the total sea level. Steric sea level changes are the second-largest trend contributor, with a rise of 1.2 mm/yr or 23% to the total. Glaciers and ice caps mass loss, terrestrial water storage decrease, and increased dynamical loading from atmospheric and oceanic non-tidal fields contribute 13% (0.7 mm/yr), 9% (0.5 mm/yr), and -1% (-0.1mm/yr) to the total trend, respectively. In terms of inter-annual variability, steric sea level and terrestrial water storage are the top two contributors (Figure 3.21). Nevertheless, over 20012-2015, the steric sea level significantly differs from the total sea level yearly variations. Contributions from land ice and atmospheric and oceanic non-tidal loading are marginal. We find a root mean squared error (RMSE) of 13.5 between the sum of sea level components with sea surface height.

In the Indian Ocean 3.1, the trend of the sum of individual sea level components and sea surface height agree within 39% (i.e., 4.3 mm/yr from the sum v.s. 3.1 mm/yr from sea surface height) (Figure 3.22). Ice sheets mass loss is leading the trend over the 15 years, with a much larger contribution of 1.7 mm/yr or 55% to the total sea level. Steric sea level changes are the second-largest trend contributor, with a rise of 1.4 mm/yr or 45% to the total. Glaciers and ice caps mass loss, terrestrial water storage decrease, and increased dynamical loading from atmospheric and oceanic non-tidal fields contribute 25% (0.8 mm/yr), 20% (0.6 mm/yr), and -8% (-0.2mm/yr) to the total trend, respectively. In terms of inter-annual variability, steric sea level and terrestrial water storage are the top two contributors, with steric sea level being dominant throughout the 15 years (Figure 3.23). Contributions from land ice and atmospheric and oceanic non-tidal loading are still marginal. We find a root mean squared error (RMSE) of 20.5 between the sum of sea level components with sea surface height.

3.5 Discussion

The level of closure in the sea level budget differs at the global mean and ocean basin mean scales. At the global mean and the Pacific Ocean basin averaged level, the sum of the individual sea level contributions has an excellent agreement in the trend and RMS with total sea level represented by altimetry measured sea surface height. However, in the Atlantic Ocean and the Indian Ocean, the trends and RMS from the sum of sea level fingerprints and steric sea level (i.e., equivalent to the sum of individual sea level contributions) differ significantly from the sea surface height. The different level of closure is possibly due to a compensation of errors from different ocean regions. The misfit in the Indian Ocean basin and the Atlantic Ocean basin may result from uncertain contribution from land water as well as warming in the deep ocean. It is also possible that the trend uncertainties in the sea surface height measurement various across ocean basins.

Although the percentage trend contribution from individual sea level components to the total sea level varies from basin to basin and from global mean to basin mean level due, this variation mainly stems from a spatial variation in the trend of sea surface height. The relative contribution between individual sea level contributions remains almost the same, with a percentage contribution from the ice sheets, steric, glaciers and ice caps, terrestrial water storage, and atmospheric and oceanic non-tidal loading 39±0.8%, 31±0.4%, 18±0.8%, and -2.5±0.9%. To obtain these percentage contributions, we first compare the trend contribution from individual sea level components to the sum of sea level components within each ocean basin and at the global mean level. Then for each sea level component, we take the average of its contributions to different ocean basins and the global mean scale. The associated error for each sea level component is calculated as the standard deviation of its trend contributions to different ocean basins and the global mean level. Therefore the errors are corresponding to a 68% confidence level.

3.6 Conclusions

We evaluate the sea level budget over the GRACE and GRACE-FO period from 2005 to 2019 using multiple satellite and in-situ measurements. We compare the sum from individual sea level components, including steric sea level, land ice and water mass changes induced sea level fingerprint, atmospheric and oceanic non-tidal loading induced sea level fingerprint, with total sea surface height measurement by altimetry. Ice sheets mass loss and steric expansion are leading to the rise in the total sea level for the past 15 years.

At the global mean scale, the sum of individual contributions and the total sea level agree within 6% in their trends. At the regional level, the level of closure varies from 7% in the Pacific Ocean, 30% in the Atlantic Ocean, to 39% in the Indian Ocean. Uncertainties in the sea surface height measurement and terrestrial water storage are the major causes of the imbalance at the basin scale. Further studies are needed to quantify human impacts on land water storage and its impacts on global and regional sea level budgets. titlesec

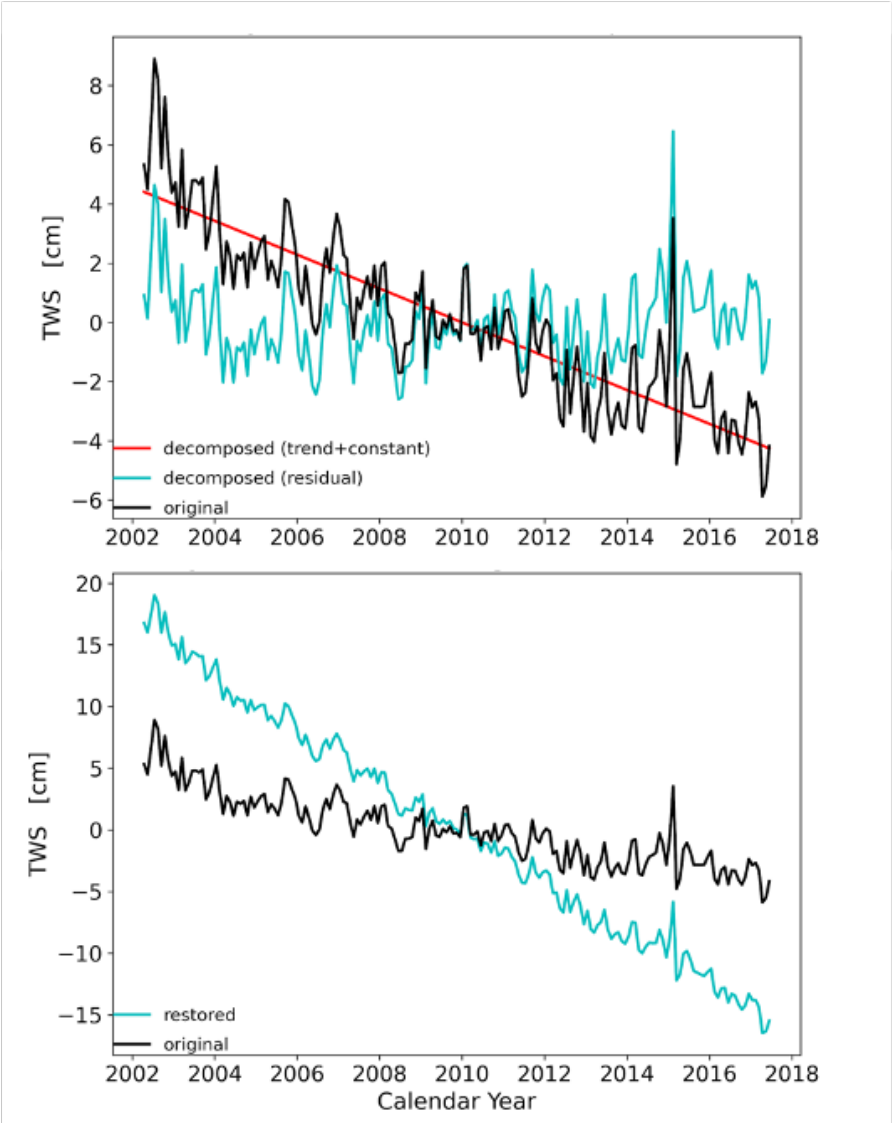

Figure 3.6: Decompose of GRACE TWS time series at Riyadh (a) and a comparison of the restored signal to the original signal from GRACE TWS at the same location.

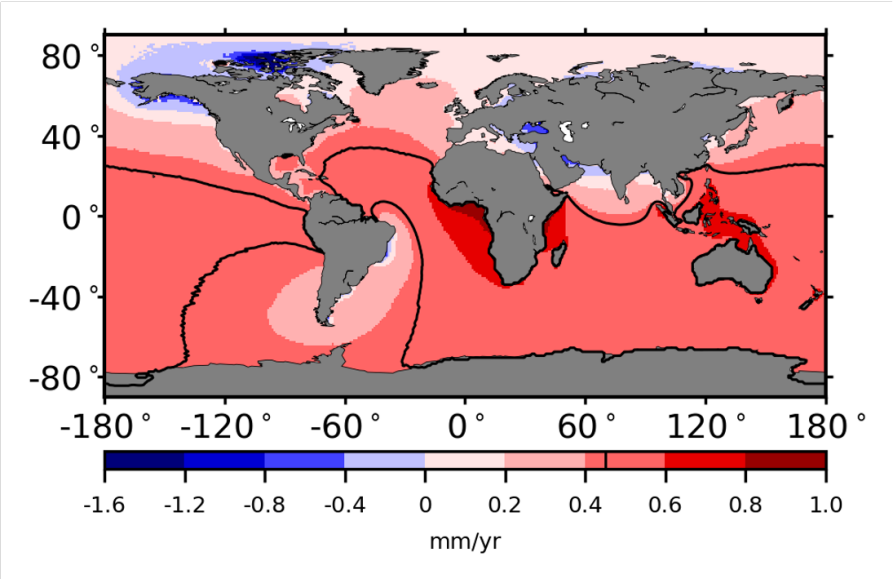

Figure 3.7: SLF trend caused by TWS mass changes over 2002-2019. Black contour line is the global mean equivalent SLF trend of 0.45 mm/yr.

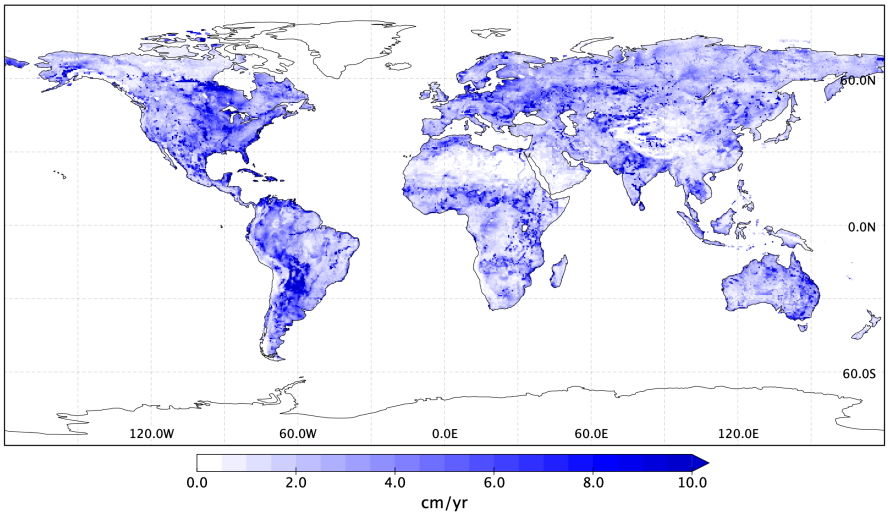

Figure 3.8: TWS error on trend due to uncertainties in the long-term scaling factors.

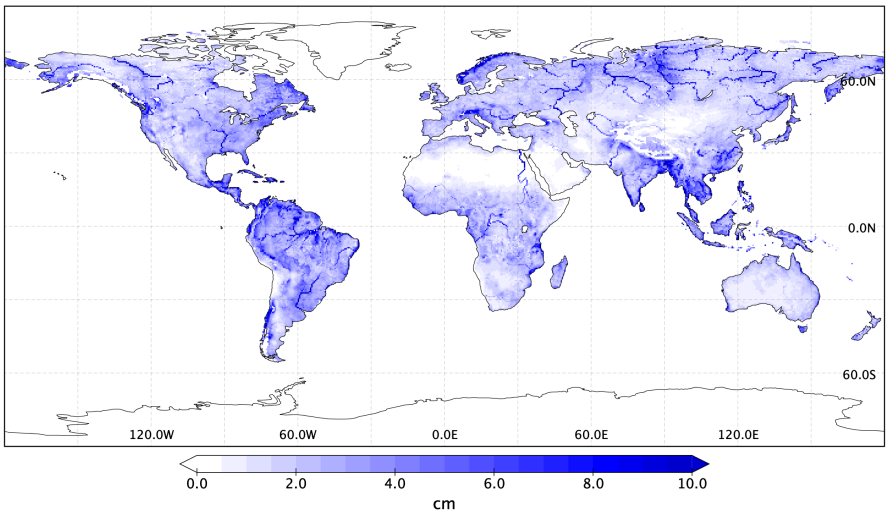

Figure 3.9: TWS error on residuals (i.e., inter-annual, annual, sub-annual signals) due to uncertainties in the residual scaling factors.

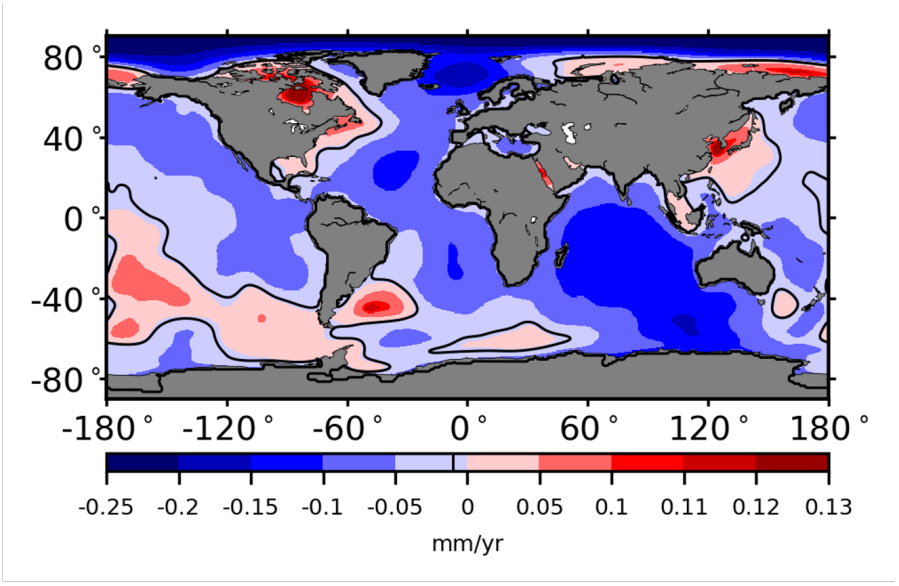

Figure 3.10: SLF trend caused atmospheric ocean non-tidal loading with a truncation up to degree 60. The black contour lines indicates a global averaged sea level trend as -0.01 mm/yr.

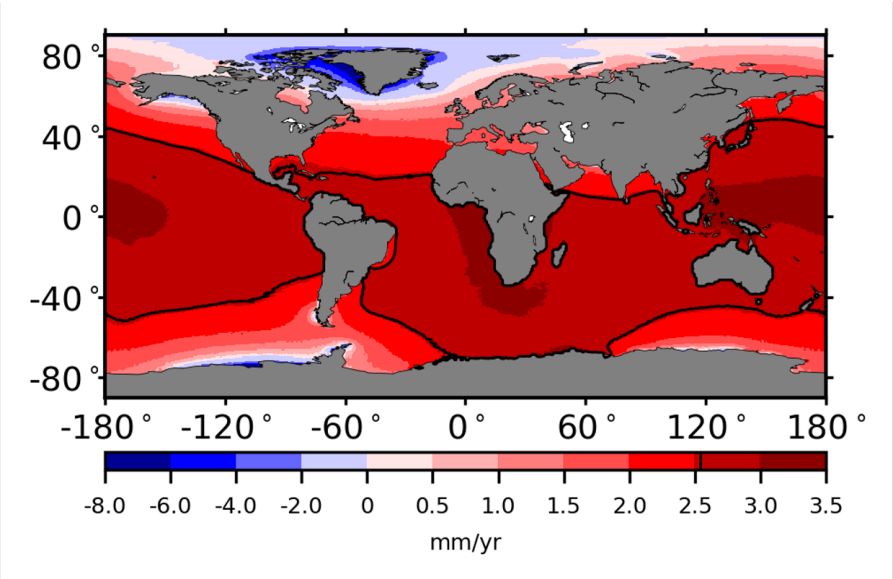

Figure 3.11: Total SLF trend caused by all land mass variations from mass variations in Greenland and Antarctic ice sheets, glaciers and ice caps (GIC), terrestrial water storage (TWS), and atmospheric and non-tidal ocean loading (AOL). The black contour lines indicates a global averaged sea level trend as 2.54 mm/yr.

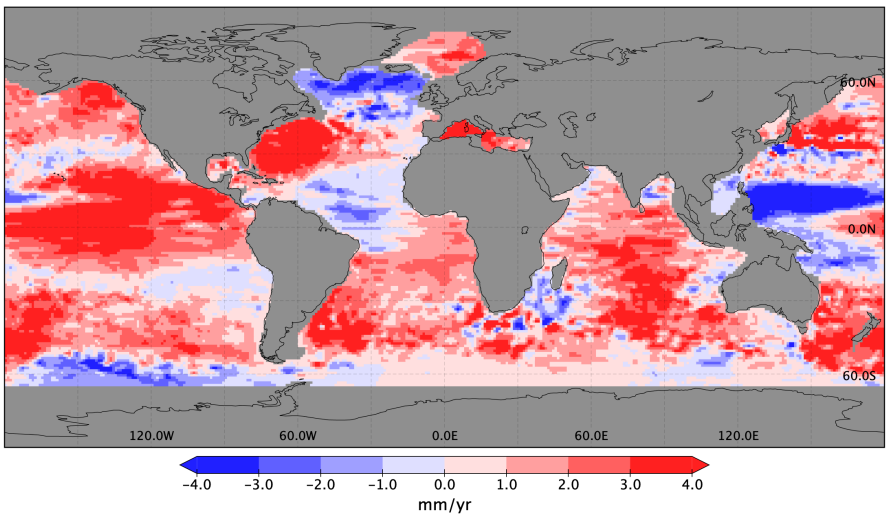

Figure 3.12: Trend of the steric sea level based on ARGO monthly fields from 2005 to 2019.

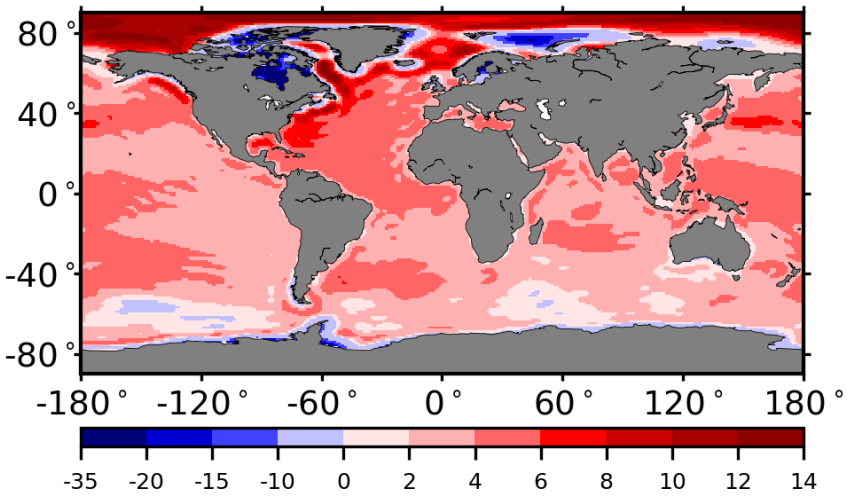

Figure 3.13: Trend of the sea surface height from 2005 to 2019. We applied GRACE-processing to sea surface height and corrected the GIA and pole tide signal before calculating trend.

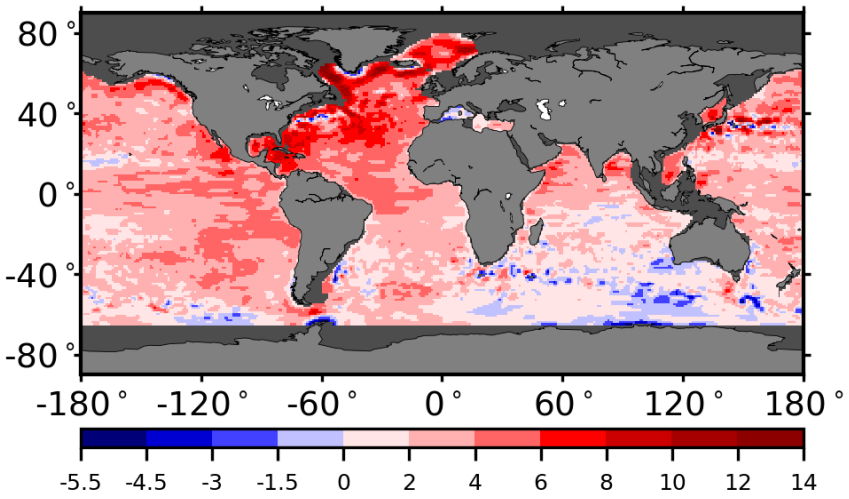

Figure 3.14: Trend of total sea level over 2002-2019 without steric sea level signal.

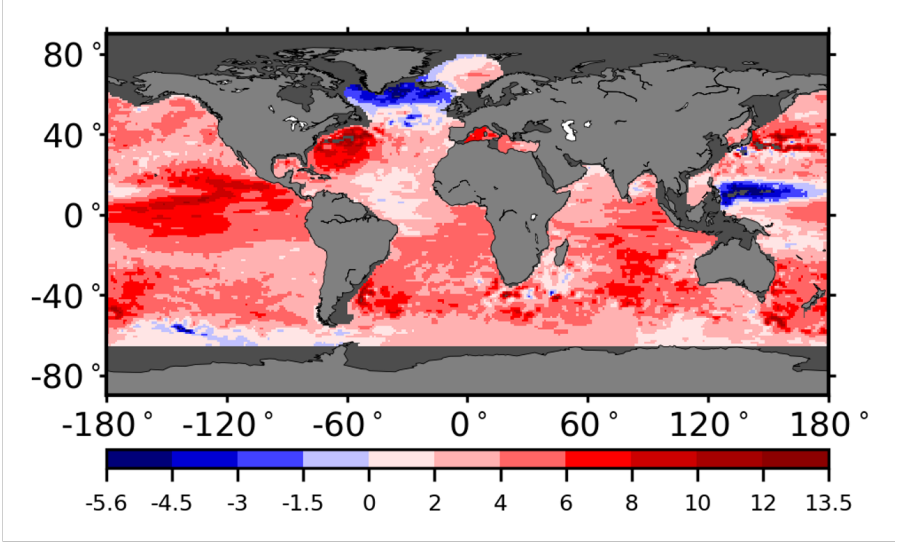

Figure 3.15: Trend of the sum of total sea level fingerprints and steric sea level over 2005-2019.

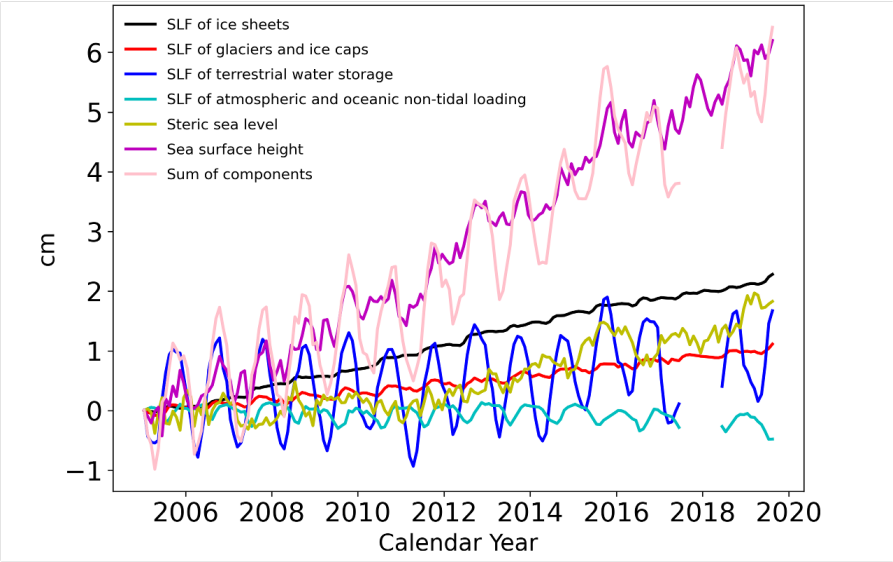

Figure 3.16: Monthly time series of global mean sea level components over January 2005 to August 2019. To compare the trends, we set the the month's sea level as zero for all sea level components.

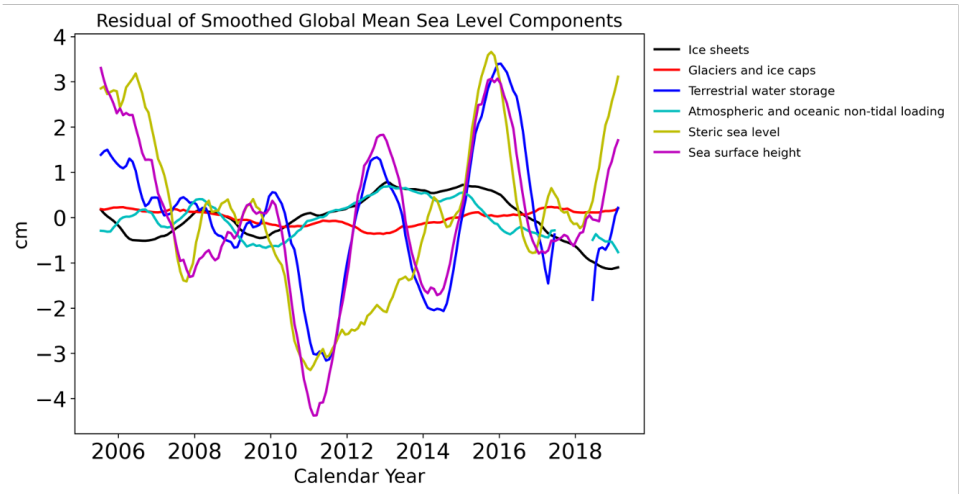

Figure 3.17: Monthly time series of smoothed residual of global mean sea level components over January 2005 to August 2019.

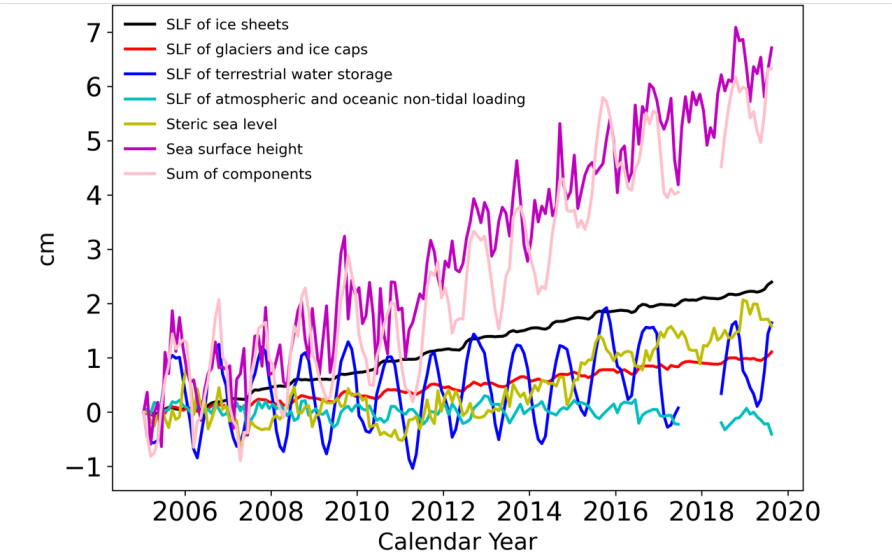

Figure 3.18: Pacific Ocean basin averaged mean sea level components monthly time series over January 2005 to August 2019.

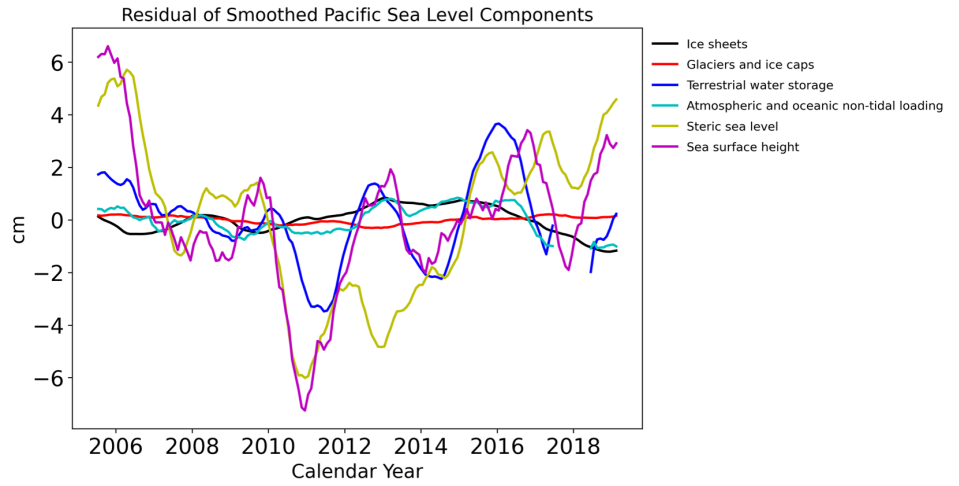

Figure 3.19: Monthly time series of smoothed residual of Atlantic Ocean basin averaged sea level components over January 2005 to August 2019.

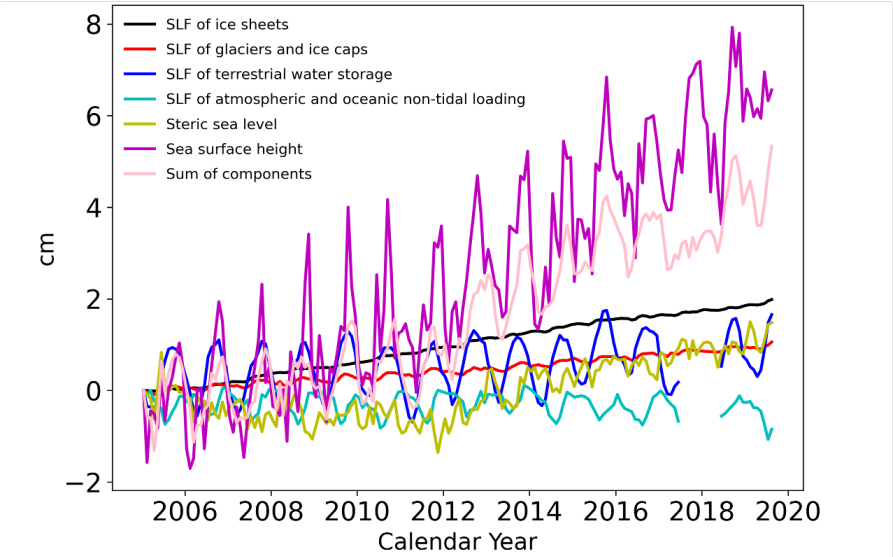

Figure 3.20: Atlantic Ocean basin averaged mean sea level components monthly time series over January 2005 to August 2019.

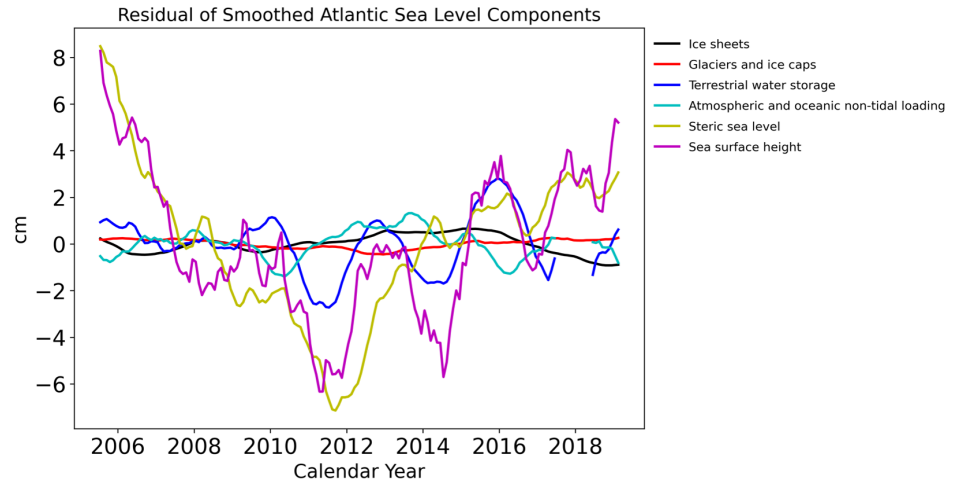

Figure 3.21: Monthly time series of smoothed residual of Atlantic Ocean basin averaged sea level components over January 2005 to August 2019.

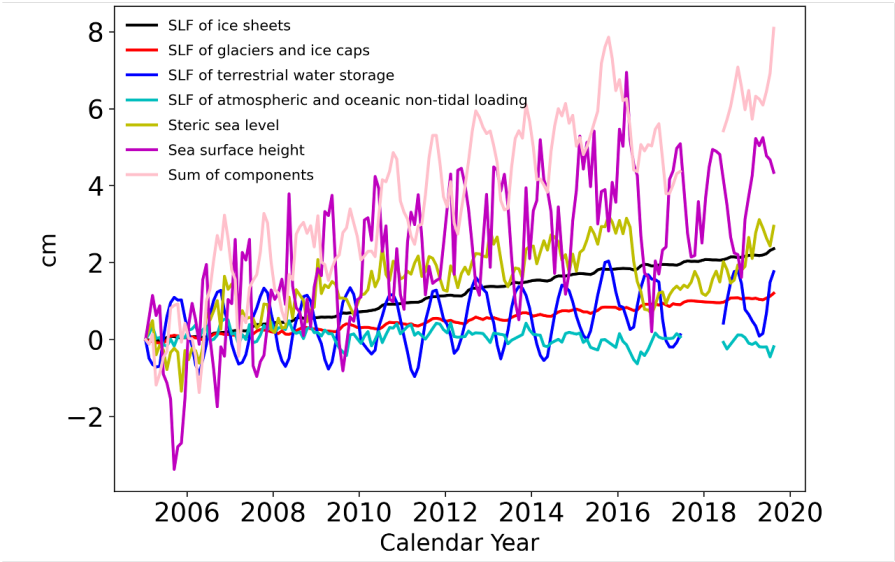

Figure 3.22: Indian Ocean basin averaged mean sea level components monthly time series over January 2005 to August 2019.

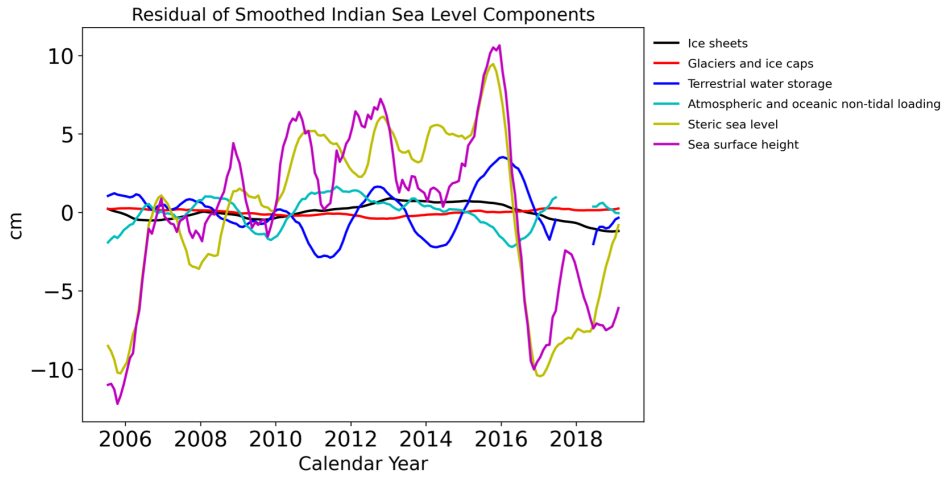

Figure 3.23: Monthly time series of smoothed residual of Indian Ocean basin averaged sea level components over January 2005 to August 2019.

Chapter 4

Conclusions

The dissertation studies the contemporary global and regional sea level changes based on satellite observations and climate model outputs. Sea level fingerprints (SLFs) of land-ice mass loss have contributed significantly to regional sea level patterns. As land-ice mass loss accumulates, the land-ice SLF signals will become increasingly dominant in the total relative sea level. Accurate trend projections of the SLFs are essential to decision-makers. Projections are often derived from model simulations, where measurement-based historical trends provide critical constraints. Ideally, a reliable time scale for trend estimation would be at least several years. However, most measurement-based trend estimations of land ice-SLFs were derived in the 1990s due to the availability of satellites measurements. Geodetic records of ice mass changes are usually long enough for trend estimates but subject to temporal and spatial scarcities.

To evaluate long-term historical land ice mass changes contributions to sea level, we reconstruct a forty-year record of land ice mass changes from 1980 to 2019. We combine forty decades of observations of ice sheet mass balance for Antarctica and Greenland and surface mass balance reconstructions of the glacier and ice caps mass balance (GIC) from 1980 to

the present. With the reconstructed land-ice mass changes record, we can determine the contribution to regional and global sea level changes from melting land ice. We estimate SLFs trends based on our reconstructed land ice mass changes. We provide uncertainties of the SLFs reconstructions. We compare the sea level rise due to SLFs at some of the world's most densely populated coastal cities to illustrate the application of this method for evaluating risks of regional sea-level rise.

Then we focus on the last 15 years of the land ice SLF record from 2005 to 2019 and combine with other sea level components to evaluate the closure of sea level budget during this period. We use altimetry-measured sea surface height as the total sea level. We calculate and process data for other individual sea level contributors from various forms of observations. For instance, we calculate the steric sea level using temperature and salinity data collected by the ARGO floats. We quantify sea level changes caused land water mass variations and atmospheric and oceanic non-tidal loading using GRACE and GRACE-FO data. We evaluate the closure of the sea level budget at the global and regional scale by comparing the sum of individual components to the total sea surface height.

4.1 Summary of Results

In Chapter 2, we present a 40-year record of land-ice mass changes from the world's major GIC, Greenland, and Antarctica that combines GRACE/GRACE-FO data, MERRA-2/GEOS-5 data, multiple other regional and global climate model outputs, and reconstructions of ice discharge from the marine-terminating glaciers in Greenland and Antarctica, that triples the observation period of SLF compared to the previous estimates based on GRACE/GRACE-FO alone, with improved confidence in the estimates during the common period. Overall, the GIC contributed a larger mass loss than Greenland and Antarctica, but the difference between them is small. The contribution of ice sheets has been rapidly

accelerating. It now dominates the sea level signal, so that over the last four decades, the three components have contributed almost equally to total sea level change. At present, the dominant signal is from the ice sheets but the GIC signal remains significant and cannot be ignored. We expect the 40-year SLF record to be of importance for comparison with other land observations to better understand the components of sea level change and its geographic distribution and help improve future sea level change projections.

Chapter 3 evaluates the sea level budget over the GRACE and GRACE-FO period from 2005 to 2019 using multiple satellite and in-situ measurements. At the global mean scale, the sum of individual contributions and the total sea level agree within 6% in their trends. At the regional level, the level of closure varies from 7% in the Pacific Ocean, 30% in the Atlantic Ocean, to 39% in the Indian Ocean. At both the global and regional scale, ice sheet mass loss is leading the trend over the 15 years and contributing to 55% to the total sea level. Steric sea level changes are the second-largest trend component which contributes to 45% of the sea level rise. In terms of inter-annual variability, the steric sea level and terrestrial water storage are the top two contributors, with the steric sea level dominant throughout the 15 years. Contributions from land ice and atmospheric and oceanic non-tidal loading are relatively small.

4.2 Implications

Our forty-year-long record of land ice mass changes can serve as a benchmark for climate models. The record can help diagnose model processes and parameters on various time scales, ranging from monthly to decadal time scales. For glaciers and ice caps that only have surface mass balance processes or where ice dynamical processes are negligible, our reconstructed GIC time series provide the true mass balance conditions for 1980-2019. The actual condition will give critical feedback to the global and regional climate models. For

instance, modelers can use the true mass balance to calibrate model parameters and constrain physical processes, such as albedo and glacier geometries. The true mass balance can also constrain past atmospheric conditions, such as air temperature and precipitation, used in models to simulate surface mass balance but lack reliable measurements in many mountain regions. The constrained atmospheric conditions will help improve the accuracy of surface mass balance model outputs and be useful for other research in mountain regions where observational data were sparse.

In constructing the forty-year land ice and the associated sea level fingerprint record, we combine the strengths of the GRACE/GRACE-FO and model datasets, which are the accuracy of satellite measurement and the long temporal coverage of the model to build a consistent, long time series with robust error budget analysis. We thoroughly accounted for errors from various sources. We quantified uncertainties in physical processes, processing procedures, and statistical error that may impact the GRACE trend estimate, and therefore could propagate on to our forty-year trend through the calibration. Those processes include, for example, glacial isostatic adjustment (GIA), post-Little Ice Age (LIA) isostatic rebound, hydrology correction, and others. We also further evaluated the uncertainties in the long-term trend and cumulative mass loss when using the MERRA-2 model for all glacier regions. We found the uncertainties are minimal compared to signals less than 6.5%. This reconstructed dataset will be maintained and regularly updated as new monthly data from GRACE-FO, MERRA-2, and MBM data becomes available. We expect the errors to be even more minor for future land ice and SLF records with the continued improvement in the three datasets.

Our long-term land ice and SLF records with the robust error budget analysis enable rigorous comparison across different datasets and increase confidence in using our product. When comparing our forty-year SLF at coastal regions with a previous thirteen-year study ([*Rietbroek et al.*, 2016], see their figure 2 and our figure 2.11) from 2002-2014 using GRACE data

alone for land ice, we find differences in the relative contributions from GIC, Greenland, and Antarctica. We observed a relatively equal contribution from these three land ice sources at our selected coastal cities. *Rietbroek et al.* [2016] has a more considerable contribution from Greenland, about 50% to the total land-ice-induced SLF at similar coastal regions (e.g., Southeast Asia), and a smaller contribution from Antarctica, which is significantly less than 30%. A larger contribution from Greenland over the recent decades is expected since the Greenland ice sheet has accelerated dramatically since the 1990s. However, the much smaller contribution from Antarctica in *Rietbroek et al.* [2016] differs from our results. We observed a significant acceleration (i.e., -8.0 Gt per year squared) in Antarctica over the past four decades, which should increase Antarctica's contribution to over 1/3 of the total. The difference likely results from uncertainties in the Glacial Isostatic Adjustment (GIA) correction applied in *Rietbroek et al.* [2016]. We expect to see more reconciled results on the Antarctic ice sheet's contribution to global and regional sea level when new methods to estimate GIA on East Antarctica accurately become available.

4.3 Future Directions

Previous work on the sea level budget analysis primarily focused on the global scale and the long-term trend (citepcazenave2018contemporary, cazenave2018global, dangendorf2017reassessment). It is also worthy of reassessing the sea level budget at the regional scales and various temporal scales for the recent decades with updated observations from GRACE and GRACE-FO, ARGO floats, Altimetry and others. Investigating the sea level budget at the annual scale will provide detailed temporal evolution of sea level from year to year. It is also important to delve into processes that caused the budget imbalance at basin scales in recent years. The largest uncertainties are expected to come from potential deep ocean warming and human impact on land water storage. Future studies should prioritize quantifying their contributions

and errors.

One interesting future work would be detecting sea level fingerprints from the tide gauges records. Detection means to unambiguously attribute part of the signal from the total sea level to sea level fingerprints. The theory of sea level fingerprint is well accepted ever since the 1970s [*Farrell and Clark*, 1976] but observational evidence of the phenomena is rare. Detection on the seasonal cycle was achieved by *Hsu and Velicogna* [2017] in 2017 using GRACE-derived SLF and ocean bottom pressure data. However, detecting trend and acceleration at the millimeter per year order was not feasible. This is due to a low signal-to-noise ratio from a relatively short time series that hindered a confident attribution of trend and acceleration in total sea level to SLF. Now we constructed a forty-year SLF record, together with robust error analysis. The extended record will enable the detection of SLF on the trend and acceleration of total sea level, which would be exciting as we will provide new observational evidence on this intriguing ocean phenomenon.

It is also important to separate impacts on regional sea-level changes from natural variability and human activities and compare the role of these two aspects on longer-term and shorter-term sea level rise. The separation will help benchmark and calibrate model processes on physical and societal modules, eventually enhancing future sea level rise prediction accuracy. Precise sea level predictions at the localized scale will be instrumental in informing coastal adaptation and mitigation.

Bibliography

Ablain, M., A. Cazenave, G. Valladeau, and S. Guinehut, A new assessment of the error budget of global mean sea level rate estimated by satellite altimetry over 1993–2008, *Ocean Science*, *5*(2), 193–201, 2009.

Adhikari, S., E. R. Ivins, T. Frederikse, F. W. Landerer, and L. Caron, Sea-level fingerprints emergent from grace mission data., *Earth System Science Data*, *11*(2), 2019.

Bamber, J. L., R. E. Riva, B. L. Vermeersen, and A. M. LeBrocq, Reassessment of the potential sea-level rise from a collapse of the west antarctic ice sheet, *science*, *324*(5929), 901–903, 2009.

Barnoud, A., et al., Contributions of altimetry and argo to non-closure of the global mean sea level budget since 2016, *Geophysical Research Letters*, *48*(14), e2021GL092,824, 2021.

Bettadpur, S., Utcsr level-2 processing standards document, *Technical Version*, *4*, 2012.

Boy, J.-P., L. Longuevergne, F. Boudin, T. Jacob, F. Lyard, M. Llubes, N. Florsch, and M.-F. Esnoult, Modelling atmospheric and induced non-tidal oceanic loading contributions to surface gravity and tilt measurements, *Journal of Geodynamics*, *48*(3-5), 182–188, 2009.

Catania, G., L. Stearns, D. Sutherland, M. Fried, T. Bartholomaus, M. Morlighem, E. Shroyer, and J. Nash, Geometric controls on tidewater glacier retreat in central western greenland, *J. Geophys. Res.: Earth Surface*, *123*(8), 2024–2038, 2018.

Cazenave, A., H. Palanisamy, and M. Ablain, Contemporary sea level changes from satellite altimetry: What have we learned? what are the new challenges?, *Advances in Space Research*, *62*(7), 1639–1653, 2018a.

Cazenave, A., et al., Global sea-level budget 1993-present, *Earth System Science Data*, *10*(3), 1551–1590, 2018b.

Chao, B. F., Y.-H. Wu, and Y. Li, Impact of artificial reservoir water impoundment on global sea level, *science*, *320*(5873), 212–214, 2008.

Chen, W., J. Luo, J. Ray, N. Yu, and J. C. Li, Multiple-data-based monthly geopotential model set ldcmgm90, *Scientific data*, *6*(1), 1–9, 2019.

Cheng, M., and J. Ries, The unexpected signal in grace estimates of c_{20}, *Journal of Geodesy*, *91*(8), 897–914, 2017.

Church, J. A., et al., Revisiting the earth's sea-level and energy budgets from 1961 to 2008, *Geophys. Res. Lett.*, *38*(18), 2011.

Ciracì, E., I. Velicogna, and S. Swenson, Continuity of the mass loss of the world's glaciers and ice caps from the grace and grace follow-on missions, *Geophysical Research Letters*, *47*(9), e2019GL086,926, 2020.

Clark, J., and C. S. Lingle, Future sea-level changes due to west antarctic ice sheet fluctuations, *Nature*, *269*(5625), 206–209, 1977.

Clark, J., and J. Primus, Sea-level changes resulting from future retreat of ice sheets: an effect of co2 warming of the climate, *Sea-level changes*, *356*, 370, 1987.

Conrad, C. P., and B. H. Hager, Spatial variations in the rate of sea level rise caused by the present-day melting of glaciers and ice sheets, *Geophysical Research Letters*, *24*(12), 1503–1506, 1997.

Csatho, B. M., et al., Laser altimetry reveals complex pattern of greenland ice sheet dynamics, *Proceedings of the National Academy of Sciences*, *111*(52), 18,478–18,483, 2014.

Davis, J. L., and N. T. Vinogradova, Causes of accelerating sea level on the east coast of north america, *Geophys. Res. Lett.*, *44*(10), 5133–5141, 2017.

De Woul, M., and R. Hock, Static mass-balance sensitivity of arctic glaciers and ice caps using a degree-day approach, *Annals of Glaciology*, *42*, 217–224, 2005.

Desai, S., J. Wahr, and B. Beckley, Revisiting the pole tide for and from satellite altimetry, *Journal of Geodesy*, *89*(12), 1233–1243, 2015.

Dobslaw, H., I. Bergmann-Wolf, R. Dill, L. Poropat, M. Thomas, C. Dahle, S. Esselborn, R. König, and F. Flechtner, A new high-resolution model of non-tidal atmosphere and ocean mass variability for de-aliasing of satellite gravity observations: Aod1b rl06, *Geophysical Journal International*, *211*(1), 263–269, 2017.

Döll, P., H. Douville, A. Güntner, H. M. Schmied, and Y. Wada, Modelling freshwater resources at the global scale: challenges and prospects, *Surveys in Geophysics*, *37*(2), 195–221, 2016.

Dyurgerov, M. B., and M. F. Meier, Twentieth century climate change: evidence from small glaciers, *Proceedings of the National Academy of Sciences*, *97*(4), 1406–1411, 2000.

Fagiolini, E., F. Flechtner, M. Horwath, and H. Dobslaw, Correction of inconsistencies in ecmwf's operational analysis data during de-aliasing of grace gravity models, *Geophysical Journal International*, *202*(3), 2150–2158, 2015.

Farrell, W., and J. A. Clark, On postglacial sea level, *Geophysical Journal International*, *46*(3), 647–667, 1976.

Fettweis, X., J. E. Box, C. Agosta, C. Amory, C. Kittel, C. Lang, D. van As, H. Machguth, and H. Gallée, Reconstructions of the 1900–2015 greenland ice sheet surface mass balance using the regional climate mar model, *The Cryosphere*, *11*(2), 1015–1033, 2017.

Frederikse, T., et al., The causes of sea level rise since 1900., *Nature*, *54*, 2020a.

Frederikse, T., et al., The causes of sea-level rise since 1900, *Nature*, *584*(7821), 393–397, 2020b.

Frezzotti, M., A. Cimbelli, and J. G. Ferrigno, Ice-front change and iceberg behaviour along oates and george v coasts, antarctica, 1912-96, *Ann. Glaciol.*, *27*, 643–650, 1998.

Gelaro, R., et al., The modern-era retrospective analysis for research and applications, version 2 (merra-2), *Journal of climate*, *30*(14), 5419–5454, 2017.

Gomez, N., J. X. Mitrovica, M. E. Tamisiea, and P. U. Clark, A new projection of sea level change in response to collapse of marine sectors of the antarctic ice sheet, *Geophysical Journal International*, *180*(2), 623–634, 2010.

Hamlington, B. D., et al., Understanding of contemporary regional sea-level change and the implications for the future, *Rev. Geophys.*, *58*(3), e2019RG000,672, 2020.

Hsu, C.-W., and I. Velicogna, Detection of sea level fingerprints derived from grace gravity data, *Geophys. Res. Lett.*, *44*(17), 8953–8961, 2017.

Hughes, C. W., M. E. Tamisiea, R. J. Bingham, and J. Williams, Weighing the ocean: Using a single mooring to measure changes in the mass of the ocean, *Geophysical research letters*, *39*(17), 2012.

Huss, M., and R. Hock, A new model for global glacier change and sea-level rise, *Frontiers in Earth Science*, *3*, 54, 2015.

Jacob, T., J. Wahr, W. T. Pfeffer, and S. Swenson, Recent contributions of glaciers and ice caps to sea level rise, *Nature*, *482*(7386), 514–518, 2012.

Joughin, I., B. E. Smith, and B. Medley, Marine ice sheet collapse potentially under way for the thwaites glacier basin, west antarctica, *Science*, *344*(6185), 735–738, 2014.

Kaser, G., J. Cogley, M. Dyurgerov, M. Meier, and A. Ohmura, Mass balance of glaciers and ice caps: Consensus estimates for 1961–2004, *Geophysical Research Letters*, *33*(19), 2006.

Kopp, R. E., R. M. Horton, C. M. Little, J. X. Mitrovica, M. Oppenheimer, D. Rasmussen, B. H. Strauss, and C. Tebaldi, Probabilistic 21st and 22nd century sea-level projections at a global network of tide-gauge sites, *Earth's future*, *2*(8), 383–406, 2014.

Landerer, F. W., and S. Swenson, Accuracy of scaled grace terrestrial water storage estimates, *Water resources research*, *48*(4), 2012.

Larsen, C., E. Burgess, A. Arendt, S. O'neel, A. Johnson, and C. Kienholz, Surface melt dominates alaska glacier mass balance, *Geophys. Res. Lett.*, *42*(14), 5902–5908, 2015.

Lawrence, D. M., et al., The community land model version 5: Description of new features, benchmarking, and impact of forcing uncertainty, *Journal of Advances in Modeling Earth Systems*, *11*(12), 4245–4287, 2019.

Le Traon, P.-Y., G. Dibarboure, G. Jacobs, M. Martin, E. Rémy, and A. Schiller, Use of satellite altimetry for operational oceanography, in *Satellite altimetry over oceans and land surfaces*, pp. 581–608, CRC Press, 2017.

Leuliette, E. W., The balancing of the sea-level budget, *Current Climate Change Reports*, *1*(3), 185–191, 2015.

Leuliette, E. W., and L. Miller, Closing the sea level rise budget with altimetry, argo, and grace, *Geophysical Research Letters*, *36*(4), 2009.

Locarnini, M., et al., World ocean atlas 2018, volume 1: Temperature, 2018.

Loomis, B., K. Rachlin, and S. Luthcke, Improved earth oblateness rate reveals increased ice sheet losses and mass-driven sea level rise, *Geophysical Research Letters*, *46*(12), 6910–6917, 2019.

McDougall, T. J., and P. M. Barker, Getting started with teos-10 and the gibbs seawater (gsw) oceanographic toolbox, *SCOR/IAPSO WG*, *127*, 1–28, 2011.

McMillan, M., et al., A high-resolution record of greenland mass balance, *Geophysical Research Letters*, *43*(13), 7002–7010, 2016.

Meier, M. F., Contribution of small glaciers to global sea level, *Science*, *226*(4681), 1418–1421, 1984.

Miles, B. W., C. R. Stokes, and S. S. Jamieson, Velocity increases at cook glacier, east antarctica linked to ice shelf loss and a subglacial flood event., *The Cryosphere.*, *12*(10), 3123–3136, 2018.

Millan, R., J. Mouginot, and E. Rignot, Mass budget of the glaciers and ice caps of the queen elizabeth islands, canada, from 1991 to 2015, *Environ. Res. Lett.*, *12*(2), 024,016, 2017.

Milne, G. A., and J. X. Mitrovica, Postglacial sea-level change on a rotating earth: first results from a gravitationally self-consistent sea-level equation, *Geophys. J. Int.*, *126*(3), F13–F20, 1996.

Mitrovica, J. X., M. E. Tamisiea, J. L. Davis, and G. A. Milne, Recent mass balance of polar ice sheets inferred from patterns of global sea-level change, *Nature*, *409*(6823), 1026–1029, 2001.

Mitrovica, J. X., N. Gomez, and P. U. Clark, The sea-level fingerprint of west antarctic collapse, *Science*, *323*(5915), 753–753, 2009.

Mitrovica, J. X., N. Gomez, E. Morrow, C. Hay, K. Latychev, and M. Tamisiea, On the robustness of predictions of sea level fingerprints, *Geophys. J. Int.*, *187*(2), 729–742, 2011.

Mohajerani, Y., I. Velicogna, and E. Rignot, Mass loss of totten and moscow university glaciers, east antarctica, using regionally optimized grace mascons, *Geophys. Res. Lett.*, *45*(14), 7010–7018, 2018.

Mohajerani, Y., I. Velicogna, and E. Rignot, Evaluation of regional climate models using regionally optimized grace mascons in the amery and getz ice shelves basins, antarctica, *Geophys. Res. Lett.*, *46*(23), 13,883–13,891, 2019.

Morlighem, M., et al., Bedmachine v3: Complete bed topography and ocean bathymetry mapping of greenland from multibeam echo sounding combined with mass conservation, *Geophys. Res. Lett.*, *44*(21), 11–051, 2017.

Morlighem, M., et al., Deep glacial troughs and stabilizing ridges unveiled beneath the margins of the antarctic ice sheet, *Nature Geosci.*, *13*(2), 132–137, 2020.

Mouginot, J., and E. Rignot, Ice motion of the patagonian icefields of south america: 1984–2014, *Geophys. Res. Lett.*, *42*(5), 1441–1449, 2015.

Mouginot, J., E. Rignot, A. A. Bjørk, M. Van Den Broeke, R. Millan, M. Morlighem, B. Noël, B. Scheuchl, and M. Wood, Forty-six years of greenland ice sheet mass balance from 1972 to 2018, *Proc. Nat. Acad. Sci.*, *116*(19), 9239–9244, 2019.

Noël, B., W. J. van de Berg, S. Lhermitte, B. Wouters, N. Schaffer, and M. R. van den Broeke, Six decades of glacial mass loss in the canadian arctic archipelago, *¿ Geophys. Res.: Earth Surface*, *123*(6), 1430–1449, 2018a.

Noël, B., et al., Modelling the climate and surface mass balance of polar ice sheets using racmo2-part 1: Greenland (1958-2016), *The Cryosphere*, *12*(3), 811–831, 2018b.

Noël, B., et al., Low elevation of svalbard glaciers drives high mass loss variability, *Nature Comm.*, *11*(1), 1–8, 2020.

Oleson, K., et al., Technical description of version 4.5 of the community land model (clm), ncar tech, *Notes (NCAR/TN-478+ STR)*, *10*, D6RR1W7M, 2010.

Oppenheimer, M., et al., Sea level rise and implications for low lying islands, coasts and communities, 2019.

Paul Boy, J., and F. Lyard, High-frequency non-tidal ocean loading effects on surface gravity measurements, *Geophysical Journal International*, *175*(1), 35–45, 2008.

Peltier, W. R., D. Argus, and R. Drummond, Space geodesy constrains ice age terminal deglaciation: The global ice-6g_c (vm5a) model, *Journal of Geophysical Research: Solid Earth*, *120*(1), 450–487, 2015.

Pfeffer, W. T., et al., The randolph glacier inventory: a globally complete inventory of glaciers, *Journal of glaciology*, *60*(221), 537–552, 2014.

Plag, H.-P., H.-U. Juettner, et al., Inversion of global tide gauge data for present-day ice load changes, 2001.

Rienecker, M. M., et al., Merra: Nasa's modern-era retrospective analysis for research and applications, *Journal of climate*, *24*(14), 3624–3648, 2011.

Rietbroek, R., S.-E. Brunnabend, J. Kusche, J. Schröter, and C. Dahle, Revisiting the contemporary sea-level budget on global and regional scales, *Proceedings of the National Academy of Sciences*, *113*(6), 1504–1509, 2016.

Rignot, E., J. Mouginot, and B. Scheuchl, Ice flow of the antarctic ice sheet, *Science*, *333*(6048), 1427–1430, 2011.

Rignot, E., J. Mouginot, B. Scheuchl, M. van den Broeke, M. J. van Wessem, and M. Morlighem, Four decades of antarctic ice sheet mass balance from 1979–2017, *Proc. Nat. Acad. Sci.*, *116*(4), 1095–1103, 2019.

Riva, R. E., J. L. Bamber, D. A. Lavallée, and B. Wouters, Sea-level fingerprint of continental water and ice mass change from grace, *Geophys. Res. Lett.*, *37*(19), 2010.

Roca, M., S. Laxon, and C. Zelli, The envisat ra-2 instrument design and tracking performance, *IEEE Transactions on Geoscience and Remote Sensing*, *47*(10), 3489–3506, 2009.

Rodell, M., I. Velicogna, and J. S. Famiglietti, Satellite-based estimates of groundwater depletion in india, *Nature*, *460*(7258), 999–1002, 2009.

Roemmich, D., and J. Gilson, The 2004–2008 mean and annual cycle of temperature, salinity, and steric height in the global ocean from the argo program, *Progress in oceanography*, *82*(2), 81–100, 2009.

Shepherd, A., et al., Trends in antarctic ice sheet elevation and mass, *Geophys. Res. Lett.*, *46*(14), 8174–8183, 2019.

Shepherd, A., et al., Mass balance of the greenland ice sheet from 1992 to 2018, *Nature*, *579*(7798), 233–239, 2020.

Smith, B., et al., Pervasive ice sheet mass loss reflects competing ocean and atmosphere processes, *Science*, *368*(6496), 1239–1242, 2020.

Sørensen, L. S., A. H. Jarosch, G. Aalgeirsdóttir, V. R. Barletta, R. Forsberg, F. Pálsson, H. Björnsson, and T. Johannesson, The effect of signal leakage and glacial isostatic rebound on grace-derived ice mass changes in iceland, *Geophysical Journal International*, *209*(1), 226–233, 2017.

Sutterley, T. C., and I. Velicogna, Improved estimates of geocenter variability from time-variable gravity and ocean model outputs, *Remote Sensing*, *11*(18), 2108, 2019.

Sutterley, T. C., I. Velicogna, E. Rignot, J. Mouginot, T. Flament, M. R. Van Den Broeke, J. M. Van Wessem, and C. H. Reijmer, Mass loss of the amundsen sea embayment of west antarctica from four independent techniques, *Geophys. Res. Lett.*, *41*(23), 8421–8428, 2014.

Swenson, S., D. Chambers, and J. Wahr, Estimating geocenter variations from a combination of grace and ocean model output, *Journal of Geophysical Research: Solid Earth*, *113*(B8), 2008.

Tamisiea, M., J. Mitrovica, G. Milne, and J. Davis, Global geoid and sea level changes due to present-day ice mass fluctuations, *Journal of Geophysical Research: Solid Earth*, *106*(B12), 30,849–30,863, 2001.

Tapley, B. D., S. Bettadpur, M. Watkins, and C. Reigber, The gravity recovery and climate experiment: Mission overview and early results, *Geophysical research letters*, *31*(9), 2004.

Thomas, M., Ocean induced variations of earths rotation–results from a simultaneous model of global circulation and tides, Ph.D. thesis, Ph. D. diss., 129 pp., Univ. of Hamburg, Germany, 2002.

Tiwari, V., J. Wahr, and S. Swenson, Dwindling groundwater resources in northern india, from satellite gravity observations, *Geophysical Research Letters*, *36*(18), 2009.

Van de Wal, R., W. Boot, C. Smeets, H. Snellen, M. Van den Broeke, and J. Oerlemans, Twenty-one years of mass balance observations along the k-transect, west greenland, *Earth System Science Data*, *4*(1), 31–35, 2012.

Van Wessem, J., et al., Improved representation of east antarctic surface mass balance in a regional atmospheric climate model, *Journal of Glaciology*, *60*(222), 761–770, 2014.

Van Wessem, J. M., et al., Modelling the climate and surface mass balance of polar ice sheets using racmo2: Part 2: Antarctica (1979-2016), *The Cryosphere*, *12*(4), 1479–1498, 2018.

Velicogna, I., Increasing rates of ice mass loss from the greenland and antarctic ice sheets revealed by grace, *Geophys. Res. Lett.*, *36*(19), 2009.

Velicogna, I., and J. Wahr, Time-variable gravity observations of ice sheet mass balance: Precision and limitations of the grace satellite data, *Geophysical Research Letters*, *40*(12), 3055–3063, 2013.

Velicogna, I., T. Sutterley, and M. Van Den Broeke, Regional acceleration in ice mass loss from greenland and antarctica using grace time-variable gravity data, *Geophys. Res. Lett.*, *41*(22), 8130–8137, 2014.

Velicogna, I., et al., Continuity of ice sheet mass loss in greenland and antarctica from the grace and grace follow-on missions, *Geophysical Research Letters*, *47*(8), e2020GL087,291, 2020.

Von Schuckmann, K., et al., The copernicus marine environment monitoring service ocean state report, *Journal of Operational Oceanography*, *9*(sup2), s235–s320, 2016a.

Von Schuckmann, K., et al., An imperative to monitor earth's energy imbalance, *Nature Climate Change*, *6*(2), 138–144, 2016b.

Wada, Y., L. P. van Beek, and M. F. Bierkens, Nonsustainable groundwater sustaining irrigation: A global assessment, *Water Resources Research*, *48*(6), 2012.

Wahr, J., and S. Zhong, Computations of the viscoelastic response of a 3-d compressible earth to surface loading: an application to glacial isostatic adjustment in antarctica and canada, *Geophysical Journal International*, *192*(2), 557–572, 2013.

Wahr, J., S. Swenson, and I. Velicogna, Accuracy of grace mass estimates, *Geophysical Research Letters*, *33*(6), 2006.

Wouters, B., R. Riva, D. Lavallée, and J. Bamber, Seasonal variations in sea level induced by continental water mass: First results from grace, *Geophysical Research Letters*, *38*(3), 2011.

Zemp, M., et al., Global glacier mass changes and their contributions to sea-level rise from 1961 to 2016, *Nature*, *568*(7752), 382–386, 2019.

Zhao, M., A. Geruo, J. Zhang, I. Velicogna, C. Liang, and Z. Li, Ecological restoration impact on total terrestrial water storage, *Nature Sustainability*, *4*(1), 56–62, 2021.